



HAL
open science

Measuring Bedload Sediment Transport with an Acoustic Doppler Velocity Profiler

Koen Blanckaert, Joris Heyman, Colin D Rennie

► **To cite this version:**

Koen Blanckaert, Joris Heyman, Colin D Rennie. Measuring Bedload Sediment Transport with an Acoustic Doppler Velocity Profiler. *Journal of Hydraulic Engineering*, 2017, 143 (6), pp.04017008. 10.1061/(ASCE)HY.1943-7900.0001293 . hal-01518505

HAL Id: hal-01518505

<https://univ-rennes.hal.science/hal-01518505>

Submitted on 8 Dec 2020

HAL is a multi-disciplinary open access archive for the deposit and dissemination of scientific research documents, whether they are published or not. The documents may come from teaching and research institutions in France or abroad, or from public or private research centers.

L'archive ouverte pluridisciplinaire **HAL**, est destinée au dépôt et à la diffusion de documents scientifiques de niveau recherche, publiés ou non, émanant des établissements d'enseignement et de recherche français ou étrangers, des laboratoires publics ou privés.

1 **Measurements of bedload sediment transport with an Acoustic Doppler** 2 **Velocity Profiler (ADVP)**

3 Koen Blanckaert¹, Joris Heyman², Colin D. Rennie³

4¹ Ecological Engineering Laboratory, ENAC, Ecole Polytechnique Fédérale Lausanne, Switzerland.
5 koen.blanckaert@epfl.ch

6 Distinguished visiting researcher, University of Ottawa

7² UMR CNRS 6251, Institut de Physique de Rennes, 35042, Rennes, France ([joris.heyman@univ-](mailto:joris.heyman@univ-rennes1.fr)
8 rennes1.fr)

9³ University of Ottawa, Ottawa, ON, K1N 6N5, Canada. Email: Colin.Rennie@uottawa.ca

11 **ABSTRACT (250 words)**

12 Acoustic Doppler Velocity Profilers (ADVP) measure the velocity simultaneously in a
13 linear array of bins. They have been successfully used in the past to measure three-
14 dimensional turbulent flow and the dynamics of suspended sediment. The capability
15 of ADVP systems to measure bedload sediment flux remains uncertain. The main
16 outstanding question relates to the physical meaning of the velocity measured in the
17 region where bedload sediment transport occurs. The main hypothesis of the paper,
18 that the ADVP measures the velocity of the moving bedload particles, is validated in
19 laboratory experiments that range from weak to intense bedload transport. First, a
20 detailed analysis of the raw return signals recorded by the ADVP reveals a clear
21 footprint of the bedload sediment particles, demonstrating that these are the main
22 scattering sources. Second, time-averaged and temporal fluctuations of bedload
23 transport derived from high-speed videography are in good agreement with ADVP
24 estimates. Third, ADVP based estimates of bedload velocity and thickness of the
25 bedload layer comply with semi-theoretical expressions based on previous results. An
26 ADVP configuration optimized for bedload measurements is found to perform only
27 marginally better than the standard configuration for flow measurements, indicating
28 that the standard ADVP configuration can be used for sediment flux investigations.
29 Data treatment procedures are developed that identify the immobile-bed surface, the
30 layers of rolling/sliding and saltating bedload particles, and the thickness of the
31 bedload layer. Combining ADVP measurements of the bedload velocity with
32 measurements of particle concentration provided by existing technology would
33 provide the sediment flux.

34

35

36KEY WORDS

37bedload transport, acoustics, three-dimensional acoustic Doppler velocity profiler (3D-
38ADVP), digital videography, particle velocimetry, optical flow

39

40HIGHLIGHTS

41 1. Signature of signal, simultaneous video analysis and agreement with semi-theoretical
42 formulae demonstrate that ADVP can measure bedload velocities and bedload layer
43 thickness.

44 2. ADVP measures time-averaged and turbulent velocities of bed load particles.

45 3. ADVP analysis identifies immobile-bed surface, and layers of rolling/sliding and
46 saltating bedload.

47INTRODUCTION

48Problem definition

49Knowledge of the quantity of sediment transported in rivers is of paramount importance, for
50example for understanding and predicting morphological evolution, hazard mapping and
51mitigation, or the design of hydraulic structures like bridge piers or bank protections. In spite
52of this importance, measurement of the sediment flux is notoriously difficult, especially
53during high flow conditions when most sediment transport occurs.

54 The sediment flux per unit width can be expressed as:

$$55 \quad q_s = \int_{z_b}^{z_s} u_s c_s dz \quad (1)$$

56where z_s is the water surface level, z_b the immobile bed level, u_s the sediment velocity, and c_s
57the sediment concentration. The total sediment flux is the most relevant variable with respect
58to the river morphology. It is, however, often separated in fluxes of suspended load sediment
59transport and bedload sediment transport. Suspended load refers to sediment particles that are
60transported in the body of the flow, being suspended by turbulent eddies. Because of their
61small size – and thus their small Stokes number – suspended particles tend to follow the flow
62streamlines, and thus their velocities are close to the velocities of the turbulent flow. In
63contrast, bedload involves larger sediment particles that slide, roll and saltate on the bed, thus
64remaining in close contact with it. The friction and the frequent collisions of bedload particles
65with the granular bed reduce considerably their velocity. Because of drag forces, fluid
66velocities may also be reduced inside the bedload layer.

67 Accurate measurement of bedload transport has long been a goal of river and coastal
68scientists and engineers (e.g., Mulhoffer 1933). Conventional measurements with physical
69samplers are limited in spatial and temporal resolution, are cost prohibitive due to substantial
70manual labour, and can be difficult and/or dangerous to conduct during high channel-forming

71flows when most bed material transport occurs. Videography techniques have been developed
72for laboratory settings and well-controlled flows (Drake et al. 1988, Radice et al. 2006,
73Roseberry et al. 2012, Heyman 2014), but are hindered when intense suspended sediment
74transport occurs due to the turbidity of the water. They are particularly difficult to use in the
75field especially under high flow conditions when intense sediment transport occurs.
76Consequently, little is known about the temporal and particularly the spatial distribution of
77fluvial bedload, other than the recognition that the spatiotemporal distribution of bed material
78transport determines channel form (Ferguson et al. 1992, Church 2006, Seizilles et al. 2014;
79Williams et al. 2015).

80 Acoustic Doppler Current Profiler (ADCP) backscatter intensity and/or attenuation
81have been used to estimate suspended sediment concentration and grain size (e.g., Guerrero et
82al. 2011; Guerrero et al. 2013; Moore et al. 2013; Latosinski et al. 2014; Guerrero et al.
832016). Rennie et al. (2002), Rennie and Church (2010), and Williams et al. (2015) have used
84the bias in ADCP bottom tracking (Doppler sonar) as a measure of apparent bedload velocity.
85Due to the diverging beams of ADCP's, this technique may provide only an indication of
86bedload particle velocities averaged over the bed surface insonified by the four beams. This
87technique also does not provide the thickness and concentration of the active bedload layer,
88which are required to determine the bed load flux (Rennie and Villard 2004; Gaueman and
89Jacobson 2006).

90 ADVP's, which use beams that converge in one single area of measuring bins, have
91commonly been used to investigate turbulent flows (Figure 1). Their application range has
92recently been extended to the investigation of the dynamics of transported sediment, mainly
93transport in suspension (e.g., Crawford and Hay 1993; Thorne and Hardcastle 1997; Shen and
94Lemmin 1999; Cellino and Graf 2000; Stanton 2001; Smyth et al. 2002; Thorne and Hanes

952002, Hurther et al. 2011; Thorne et al. 2011; Thorne and Hurther 2014). The present paper
96focuses on their use for the measurement of bedload sediment transport.

97ADVP: working principle and state-of-the-art

98 The working principle of ADVP has been detailed previously (e.g., Lemmin and
99Rolland 1997 ; Hurther and Lemmin 1998; Thorne et al. 1998; Shen and Lemmin 1999;
100Stanton and Thornton 1999; Stanton 2001; Zedel and Hay 2002). The main features of the
101ADVP's working principle that are required for making the present paper self-contained are
102summarized hereafter. An ADVP consists of a central beam emit transducer surrounded by
103multiple fan-beam receive transducers (Figure 1a). The instrument is typically set up on a
104fixed mount pointing down toward the bed, and measures simultaneously velocities in the
105water column situated between the emitter and the bed. This water column is divided in
106individual bins of O(mm). The profiling range, i.e. the height of the measured water column,
107is typically of O(m). The emit transducer sends a series of short acoustic pulses vertically
108down towards the bed with a user-defined pulse-repetition-frequency (PRF) and pulse length.
109These pulses are reflected by scattering sources in the water, and a portion of this scattered
110sound energy is directed toward the receive transducers. Turbulence-induced air bubble
111microstructures in sediment-free clear water (Hurther, 2001) or sediment particles in
112sediment-laden flows (Hurther et al. 2011) can be scattering sources of this instrument. For
113each bin in the water column, the backscattered signal recorded by each of the receivers can
114be written as:

$$115 \quad a(t) = A \cos[2\pi(f_0 + f_D)t] \quad (2)$$

116A is the amplitude of the recorded signal and f_D the Doppler frequency shift. The latter is
117proportional to the velocity component directed along the bisector of the backscatter angle
118(Figure 1b):

$$f_D = 2 \frac{f_0}{c} \vec{V} \cdot \vec{e}_B \quad (3)$$

119

120The speed of sound in water is indicated by c , \vec{V} is the vectorial velocity of the scattering
 121source, \vec{e}_B the unit vector along the bisector of the backscatter angle for the considered bin.
 122In order to compute f_D , the recorded signal $a(t)$ is typically demodulated into in-phase and
 123quadrature components, represented by $I(t)$ and $Q(t)$, measured in volt. The Doppler
 124frequency $f_D(t)$ corresponds to the frequency of these oscillating $I(t)$ and $Q(t)$ signals. The
 125demodulation into in-phase and quadrature parts is necessary to determine the sign of f_D . The
 126quasi-instantaneous Doppler frequency is typically computed with the pulse-pair algorithm
 127using NPP (number of pulse-pairs) samples of $I(t)$ and $Q(t)$ (Miller and Rochwarger 1972;
 128Lhermitte and Serafin, 1984; Zedel et al. 1996; Zedel and Hay 2002):

$$\hat{f}_D = \frac{PRF}{2\pi} \tan^{-1} \left[\frac{\sum_{s=1}^{NPP-1} Q_s I_{s+1} + I_s Q_{s+1}}{\sum_{s=1}^{NPP-1} I_s I_{s+1} + Q_s Q_{s+1}} \right] \quad (4)$$

129

130The symbol $\hat{}$ denotes an average over NPP time samples, and s denotes a time index. NPP
 131has to be chosen high enough to assure second-order stationarity, but low enough so that
 132NPP/PRF remains small compared to the characteristic timescale of the investigated turbulent
 133flow. Utilization of at least three receive transducers allows for measurement of all three
 134velocity components. Beam velocities are converted to Cartesian coordinates using a beam
 135transformation matrix specific for the beam geometry.

136

[Figure 1]

137 Acoustic Concentration and Velocity Profilers (ADCP), which integrate an ADVP and
 138an Acoustic Backscatter System (ABS), have been successfully used to investigate suspended
 139sediment fluxes, defined as the product of sediment velocity and sediment concentration

140(Equation 1). The ADVP measures the velocity of the suspended sediment, which is assumed
141to be equal to the flow velocity. The ABS provides the particle concentration in bins
142throughout a profile is obtained based on the range-gated acoustic backscatter intensity and/or
143attenuation (e.g., Crawford and Hay 1993; Thorne and Hardcastle 1997; Shen and Lemmin
1441999; Thorne and Hanes 2002; Hurther et al. 2011; Thorne et al. 2011; Thorne and Hurther
1452014; Wilson and Hay 2015; Wilson and Hay 2016). These measurements have permitted
146direct examination of suspended sediment transport as a function of flow forcing. For
147example, Smyth et al. (2002) used an ADCP system to document periodic sediment
148suspension associated with turbulent vortex shedding from ripples in a wave bottom
149boundary layer.

150 A broadband multifrequency ADCP, called MFDop, capable of 0.0009 m vertical
151resolution at 85 Hz has recently been developed by Hay et al. (2012a,b,c), that allows for
152estimation of both particle concentration and grain size (Crawford and Hay 1993; Thorne and
153Hardcastle 1997; Wilson and Hay 2015; Wilson and Hay 2016). For this system, velocities
154measured in bins within 0.005 m of a fixed bed were deemed to be negatively biased, based
155on nonconformity with the profiles of both log-law velocity and phase shift expected in a
156wave bottom boundary layer. This bias occurred largely because equal travel time paths
157between send and receive transducers included bottom echo for bins close to the bed (Figure
1581a,b). However, the system was able to measure the bed velocity (of an oscillatory cart) based
159on Doppler processing of the signal at the observed bottom range.

160 Hurther et al. (2011) have recently developed ACVP, which combines an ADVP with
161advanced noise reduction for turbulence statistics (Blanckaert and Lemmin 2006, Hurther and
162Lemmin 2008) with the ABS system developed by Thorne and Hanes (2002). The ACVP
163measures co-located, simultaneous profiles of both two-component velocity and sediment
164concentration referenced to the exact position at the bed. Measurements are performed with

165high temporal (25 Hz) and spatial (bin size of 0.003 m) resolution. Sediment concentration
166profiles are determined by applying the dual-frequency inversion method (Bricault 2006;
167Hurther et al. 2011), which offers the unique advantage of being unaffected by the non-linear
168sediment attenuation across highly concentrated flow regions, and thus to allow also for the
169measurement of high sediment concentrations near the bed where the bedload transport
170occurs. The acoustic theory underpinning the dual-frequency inversion method is based on
171the condition of negligible multiple scattering (Hurther et al. 2011). Although this condition is
172probably violated in the bedload layer, Naqshband et al. (2014b, their Figure 12) have
173successfully applied the method to estimate the sediment concentration all through the
174bedload layer onto the immobile bed, where a bulk concentration of $\rho_s(1-\varepsilon) = 1590 \text{ kg m}^{-3}$
175was correctly measured. Here ε is the porosity of the immobile sediment bed. These results
176indicate that the theoretical condition of negligible multiple scattering can be relaxed and that
177the dual-frequency inversion method is also able to measure the high sediment concentrations
178in the bedload layer. The ACVP has been used to measure velocity, concentration profiles and
179sediment fluxes over ripples under shoaling waves (Hurther and Thorne 2011) and over
180migrating equilibrium sand dunes (Naqshband et al. 2014a,b). An acoustic interface detection
181method was used to identify the immobile bed and the suspended load layer and a layer in
182between with higher sediment concentrations (Hurther and Thorne 2011; Hurther et al. 2011).
183Hurther and Thorne (2011) acknowledged uncertainty in the identification of the near-bed
184layer with high sediment concentration, but found that the estimated sediment flux matched
185estimates based on ripple migration. They termed this layer the “near-bed load layer”.
186Naqshband et al. (2014b) also found that sediment fluxes in this layer were in line with
187estimates for bedload transport. Measured velocities in this layer were found to deviate from
188the logarithmic profile often observed above plane immobile beds. These deviations were
189attributed to the presence of the high sediment concentration. There remains uncertainty,

190however, in the physical meaning of the velocities measured in this non-logarithmic velocity
191layer. This uncertainty is acknowledged by Naqshband et al. (2014b), who note that it is
192difficult to validate whether this layer corresponds to the physical bedload layer, because no
193data could be collected to trace sediment movement or sediment paths.

194 These recent developments clearly demonstrate that ADCP systems are capable of
195measuring suspended load sediment flux, but that the capability of ADCP systems to measure
196bedload sediment flux remains uncertain. The ABS component of the system's ability to
197measure sediment concentration in the bedload layer has been demonstrated (Naqshband et
198al. 2014b). The main outstanding question relates to the physical meaning of the velocity
199measured by the ADV component of the system in the region where bedload sediment
200transport occurs (Equation 1).

201 Other issues remain that render uncertain the capability of ADV systems to measure
202bedload. First, 3D acoustic velocity profilers are usually configured to obtain optimal
203measurements of flow properties. Typically, an ADV is set up such that the region of overlap
204of the emit and receive beams maximizes the profiling range and includes the entire water
205column, such that optimal measurements of flow properties are obtained in the core of the
206water column (Figure 1a). This means that the axis of the receiver, where the receivers'
207sensitivity is highest, intersects theinsonified water column in a bin displaced above the bed
208in the body of the water column. Moreover, the acoustic power is optimized in the water
209column, in order to maximize the signal-to-noise ratio (SNR). This commonly leads to a
210power level of the backscatter for bins near the bed that is outside the recording range of the
211receivers, because the acoustic backscatter from bedload sediment particles is much greater
212than from scatterers in the water (Figure 2). Second, there is potential for contamination of
213near-bed bins by high intensity scatter from the immobile bed with equivalent acoustic travel
214time between the send and receive transducers (Figure 1a,b). As discussed above, this can

215result in negative bias of particle velocities estimated in near-bed bins (Hay et al. 2012a).
216This can also result in saturation of the first bin echo, which makes difficult the estimation of
217Doppler velocity and particle concentration. Similarly, highly concentrated bedload in the
218first bin can saturate the echo from the first bin. Third the nature of bedload itself renders the
219scattering and propagation within the bedload layer complex. The usual scattering model
220assumes a low concentration of scatterers in the water. This assumption is most probably
221violated in the bedload layer. Moreover, bedload particle sizes and velocities are variable,
222thus bedload transport tends to be a heterogeneous phenomenon, which broadens the received
223frequency spectrum and could render Doppler velocity estimates imprecise. Bed material
224particle size distributions tend to be log-normal, and bedload particle velocity distributions
225can be left skewed gamma (Drake et al. 1988, Rennie and Millar 2007), exponential
226(Lajeunesse et al. 2010; Furbish et al. 2012) or Gaussian (Martin et al. 2012, Ancy and
227Heyman 2014). Conventional Doppler signal processing techniques find the mean velocity in
228a presumed homogenous volume of particles, and this estimate may not best characterize the
229bedload.

230 [Figure 2]

231 **Hypothesis and detailed objectives**

232 The main objective of the present paper is to demonstrate the capability of ADV
233systems to measure bedload sediment transport, by investigating the physical meaning of the
234velocity measured with the ADV in the region where bedload sediment transport occurs. In
235all experiments without sediment transport reported in this paper, the ADV resolved the law
236of the wall logarithmic velocity profile, including very close to the bed (Figure 3a). On the
237contrary, in all experiments with bedload sediment transport reported in this paper, velocities
238in the near-bed region where bedload sediment transport occurs were found to deviate from
239the logarithmic profile (Figure 3a,b), similar to observations Naqshband et al. (2014b). The

240main hypothesis of the present paper is that the ADVP measures the velocity of the sediment
241particles moving as bedload in this near-bed region. The hypothesis is tested over a range of
242bedload transport conditions for a gravel-sand bed material mixture in a mobile bed flume. In
243this paper we focus on measurement of bedload particle velocities and the thickness of the
244bed load layer. In order to validate the hypothesis, three strategies are followed. First, a
245detailed analysis is performed of the raw $I(t)$ and $Q(t)$ signals recorded by the ADVP's
246receivers that reveals a clear footprint of the bedload sediment particles. Second,
247simultaneous observations of bedload sediment transport are conducted with high speed
248digital videography. Third, ADVP based estimates of the bedload velocities and thickness of
249the bedload layer are compared to semi-theoretical formulae based on previous results.

250 The present research makes use of an ADVP configuration that is specifically designed
251and tested for measurement of bedload transport. As described below, the instrument beam
252geometry is designed such that it is most sensitive in the first bin above the bed, and the
253acoustic power is chosen such that backscattered signal remains within the recording range of
254the receivers in the bedload region (Figure 2). The bedload measurement capabilities of this
255optimised ADVP configuration and the standard ADVP configuration for flow measurements
256are also compared.

257 [Figure 3]

258METHODS

259Experimental program

260The ADVP's potential to measure bedload was tested in a flume at École Polytechnique
261Fédéral de Lausanne (EPFL). The flume was 0.50 m wide with zero slope, and the test
262section was 6.6 m downstream of the flume inlet. The bed sediment was poorly sorted ($\sigma =$
263 $0.5 \times (d_{84}/d_{50} + d_{50}/d_{16}) = 4.15$, where d_i represents the i^{th} percentile grain size) with median,

264mean, and 90th percentile grain sizes of $d_{50}=0.0008$ m, $d_m = 0.0023$ m and $d_{90} = 0.0057$ m,
265respectively (Leite Ribiero et al. 2012). The critical shear velocity for the initiation of
266sediment transport for d_{50} and d_m are 0.020 m s⁻¹ and 0.039 m s⁻¹, respectively, based on the
267Shields criterion (Shields 1936). No sediment was fed to the flume or recirculated during the
268tests. The transported sediment originated from the entrance reach of the flume, where
269erosion locally occurred. Between experiments, the scour hole was replenished to compensate
270for sediment lost from the system. Due to the inherent intermittency and variability of
271sediment transport (Drake et al. 1988, Frey et al. 2003, Singh et al 2009; Heyman et al. 2013;
272Mettra 2014) and the formation of small dunes, bed levels varied during some of the tests.
273These conditions were chosen on purpose, in order to provide a broad range of experimental
274conditions, and to test the robustness of ADVP bedload measurement in quasi-realistic
275conditions. Table 1 summarizes the conditions in all experiments.

276 The main series of tests utilized simultaneously both the ADVP in a configuration
277optimized for the measurement of bedload transport (Figure 1b), and a digital video camera
278for bedload measurement (Figure 1c). The nominal flow depth was 0.24 m, but varied
279slightly between test runs (Table 1). This flow depth was obtained by regulating a weir at the
280downstream end of the flume. Three bedload transport conditions were tested by changing the
281flow rate in the flume. The low flow run Q630 ($Q = 0.063$ m³ s⁻¹) resulted in dune transport of
282fine sediment (smaller than d_m) that led to gradual armouring of the bed. The medium flow
283run Q795 ($Q = 0.080$ m³ s⁻¹) produced partial transport conditions, with coarser particles in
284transport, but many of the coarse particles on the bed surface were stable at any particular
285instant. Lastly, the high flow run Q1000 ($Q = 0.100$ m³ s⁻¹) broke up the armour bed and the
286entire bed surface and all grain sizes were mobile throughout the run. At these highest flow
287conditions, the saltation height and length of bedload particles were considerably increased,
288but suspended load sediment transport remained negligible. The Shields parameters based on

289 d_{50} and d_m varied from 0.07 to 0.24 and from 0.02 to 0.08, respectively, in these experiments.
290 The sediment transport behaviour was in agreement with expectations based on the Shields
291 parameter and the critical shear velocity for the different grain sizes in the sediment mixture
292 (Bose and Dey 2013). Videos of the three sediment transport conditions are available as
293 supporting information. Measurements with high and low acoustic power were utilized and
294 compared for each bedload transport condition (Figure 2). The high acoustic power
295 corresponds to the standard ADVP setting, where SNR is optimized in the main body of the
296 water column, but leads to frequent saturation of the signal in the near-bed area. The low
297 acoustic power minimizes potential for acoustic saturation of the near-bed layer. It is
298 expected to improve measurements in the near-bed layer, but leads to a lower SNR in the
299 main body of the water column. The labels of experiments with high and low acoustic power
300 are appended with H and L, respectively (Table 1).

301 [Table 1]

302 A second series of tests was also collected with the ADVP in its standard configuration
303 optimized for flow measurements in the body of the water column (Figure 1a), and without
304 simultaneous videography (Table 1). The purpose of this series was to compare the
305 capabilities of the standard ADVP configuration and the one optimized for bedload
306 measurements, and to extend the investigation to a broader range of hydraulic conditions.
307 Experiments were performed with nominal flow depths of 0.14 m and 0.24 m. For each of
308 these flow depths, 10 different discharges were tested (Table 1). In the tests with 0.14 m flow
309 depth, discharge ranged from $0.013 \text{ m}^3 \text{ s}^{-1}$ to $0.060 \text{ m}^3 \text{ s}^{-1}$, shear velocity from 0.009 m s^{-1} to
310 0.052 m s^{-1} and the Shields parameters based on d_{50} and d_m from 0.006 to 0.20 and from 0.002
311 to 0.07, respectively. In the tests with 0.24 m flow depth, discharge ranged from $0.020 \text{ m}^3 \text{ s}^{-1}$
312 to $0.100 \text{ m}^3 \text{ s}^{-1}$, shear velocity from 0.012 m s^{-1} to 0.062 m s^{-1} and the Shields parameter based
313 on d_{50} and d_m from 0.01 to 0.29 and from 0.003 to 0.10, respectively. At the lowest discharge,

314no sediment transport occurred, whereas generalized and intense sediment transport occurred
315at the highest discharge. Again, the sediment transport behaviour was as expected based on
316the Shields parameter and the critical shear velocity for the different grain sizes in the bed
317mixture (Bose and Dey 2013). The runs with 0.24 m flow depth encompassed the hydraulic
318conditions investigated in the main series with optimized ADVP configuration and
319simultaneous videography, which facilitates comparison.

320ADVP configuration and data analysis procedures

321The ADVP utilized for this research has been developed at EPFL. Its working principle has
322been detailed in Rolland and Lemmin (1997), Hurther and Lemmin (1998, 2001), Hurther
323(2001), and Blanckaert and Lemmin (2006). The instrument consists of a central emit
324transducer of diameter 0.034 m and of carrier frequency, $f_0 = 1$ MHz, with beam width of
325 1.7° , and four 30° fan-beam receive transducers that are 30° inclined from the vertical (Figure
3261). In all experiments, PRF was set to 1000 Hz, and NPP to 32, yielding a sampling frequency
327of $\text{PRF}/\text{NPP} = 31.25$ Hz for the quasi-instantaneous Doppler frequencies and velocities. A
328pulse length of $5 \mu\text{s}$ was chosen, yielding a vertical resolution of velocity bins of about 0.004
329m. A time series of more than 10 min was collected for each test condition, which was
330sufficient to obtain statistically stable measurements of the flow and sediment transport under
331 quasi-steady conditions. Blanckaert and de Vriend (2004) and Blanckaert (2010)
332discuss in detail the uncertainty in the flow quantities measured with this ADVP. They report
333a conservative estimate of 4% uncertainty in the streamwise velocity u .

334 In the main series of tests (Table 1), the ADVP configuration was optimized to measure
335bedload transport, as explained hereafter (Figure 1b). The ADVP was configured
336symmetrically, with horizontal and vertical distances between emit and receive transducers of
3370.1305 m and 0.0304 m, respectively. The ADVP was immersed in the flow, with the emit
338transducer 0.185 m above the nominal bed level. With this configuration, the centre of the

339 receive beam was focused on the bed level. This ensured that the ADV was most sensitive in
340 the vicinity of the bedload layer. This configuration, however, did not allow for
341 measurements in the upper half of the water column (Figure 1b).

342 In the second series of experiments (Table 1), the standard ADV configuration was
343 used (Figure 1a). Receivers symmetrically surrounded the emit transducer at horizontal and
344 vertical distances of 0.1343 m and 0.0295 m, respectively. In order to measure the entire
345 water column, the ADV was placed about 7 cm above the water surface in a water-filled box
346 that was separated from the flowing water with an acoustically transparent mylar film (Figure
347 1a). The box induces perturbations of the flow in a layer with a thickness of about 0.02 m near
348 the water surface. In the experiments with flow depth of 0.14 m, the center of the receive
349 beam was focused on the bed level. In the experiments with flow depth of 0.24 m, it was
350 focused in the core of the water column, about 0.10 m above the bed (Figure 1a).

351 The acoustic footprint on the bed of the emitted beam is circular with a diameter that
352 ranges from about 0.045 m in the experiments with 0.14 m flow depth to about 0.055 m in the
353 experiments with 0.24 m flow depth (Figure 1). This means that the ADV does not resolve
354 grain scale processes, but processes at a characteristic scale of about 0.05 m.

355 The standard ADV data analysis procedure considers two output quantities: the
356 magnitude of the backscattered signal recorded by the receive transducers (Figure 2) and the
357 time-averaged velocity estimated with the pulse-pair algorithm (Equation 4, Figure 3).

358 The profile of the time-averaged longitudinal flow velocity is typically logarithmic in
359 the vicinity of the bed in cases without bedload sediment transport (Nezu and Nakagawa,
360 1993). In order to identify the logarithmic part, the measured time-averaged velocity is
361 plotted as a function of $\log(30z/k_s)$, where z is the distance in meter above the immobile bed,
362 and the equivalent grain roughness k_s is taken as 0.01 m (Figure 3). In order to avoid

363 singularities, the bin containing the surface of the immobile bed has been plotted at $z = 0.001$
364 m. The profile of the time-averaged velocity as a function of $\log(30z/k_s)$ also identifies the
365 near-bed region where the measured velocities are smaller than the logarithmic profile in
366 cases with bedload sediment transport, similar to observations by Naqshband et al. (2014b).
367 In this non-logarithmic near-bed layer, the measured velocity profiles typically have an S-
368 shape (Figure 3). As mentioned before, the main hypothesis of the present paper is that the
369 ADVP measures the particle velocities in this near-bed zone. Sediment is predominantly
370 moving as bed load transport in the investigated experiments. Most particles are
371 intermittently entrained from the immobile bed by the flow, slide and roll over the immobile
372 bed, and finally immobilize again. The velocity of these sliding and rolling particles is
373 generally smaller than the velocity of the surrounding fluid, due to momentum extraction by
374 inter-particle collisions, inertia of the sediment particles, and friction on the granular bed. The
375 difference between the velocities of particles and the entraining flow is called the slip
376 velocity (Nino and Garcia 1996; Muste et al. 2009). It is assumed that the extrapolated
377 logarithmic profile provides an estimate of the velocity of the entraining flow. An increase in
378 number of moving particles can be assumed to increase the momentum extraction due to
379 inter-particle collision, and hence also the slip velocity. Therefore, the dominant bed load
380 transport is assumed to occur at the elevation of maximum slip velocity, which approximately
381 coincides with the inflection point in the S-shaped near-bed velocity profile (Figure 3b). By
382 definition, this inflection point occurs where the second derivative of the velocity with
383 respect to z vanishes. Some bedload particles saltate on the bed and reach higher elevations in
384 the water column. Because saltating bedload particles are usually relatively small and their
385 saltation length scale is longer with fewer inter-particle collisions than those of the rolling
386 bedload particles, their velocity is closer to the velocity of the entraining fluid. As mentioned
387 before, suspended load particles have negligible slip velocity and move at about the same

388velocity as the flow. Thus, the shape of the measured velocity profile identifies the layer with
389rolling and sliding bedload transport, the layer with saltating bedload transport and the layer
390with suspended load transport or clear water.

391 A critical issue in the identification of the different layers of sediment transport is the
392identification of the elevation of the surface of the immobile bed, which by definition
393corresponds to zero velocity. The accuracy in the identification of the immobile bed surface is
394limited by the finite bin size of 0.004 m and by the fact that a natural sediment bed is not
395perfectly planar. The best practice consists in identifying the bin in which the surface of the
396immobile bed is situated, as illustrated in Figure 4. The upper part of that bin will be situated
397in the flow. In case no bedload sediment transport occurs, the ADVP will measure zero
398velocity in the bin containing the surface of the immobile bed, because the magnitude of the
399raw signal backscattered on micro-air bubbles in the flowing water is much smaller than the
400magnitude of the one backscattered on the immobile bed. If bedload sediment particles roll
401and slide on the immobile bed within the bin containing the immobile bed, the ADVP will
402measure a non-zero velocity, which corresponds to the average velocity of sediment particles
403within that bin (Figure 4), i.e. this spatial average also includes areas of zero velocity
404associated with immobile particles within the measuring area of the ADVP. The bin
405containing the surface of the immobile bed is therefore identified as the bin with the
406minimum non-zero velocity, as illustrated in Figures 3 and 4.

407 A second independent estimation of the bin containing the surface of the immobile bed
408is obtained from the magnitude of the raw backscattered signal recorded by the receivers, $I^2 =$
409 $0.25 (I_1^2 + I_2^2 + I_3^2 + I_4^2)$ (Figure 2). Here, I_1 , I_2 , I_3 and I_4 are the raw in-phase components of the
410demodulated signals recorded by each of the four receivers. The magnitude of the
411backscattered signal relates to the concentration of the sediment particles, because sediment
412particles backscatter considerably more acoustic energy than micro air-bubbles in the water

413column above (Hurther et al. 2011). Based on this heuristic definition, the bin containing the
414immobile bed is assumed to correspond to the peak in the profile of the magnitude of the
415backscattered signal (Figure 2). In the present paper, we have used the first estimation to
416define the bin containing the surface of the immobile bed, and the second estimation for
417validation purposes. In general, both estimation identified the same bin.

418 In the Q795L experiment shown in Figures 2 and 3b, the surface of the immobile-bed is
419estimated within bin number 58, the sliding and rolling bedload is estimated in bin 57, and
420the top of the saltating bedload in bin 55. These heuristic estimations are based on the shape
421of the velocity profile as discussed earlier. In most experiments, however, the bed load
422sediment transport caused variations in the elevation of the surface of the immobile bed
423during the 10 min duration of the experiment. This is illustrated for experiment Q1000L in
424Figure 5, which shows the temporal evolution of the magnitude of the raw backscattered
425return signal, $I^2 = 0.25 (I_1^2 + I_2^2 + I_3^2 + I_4^2)$, during the 614 s measurement period. The figure
426highlights the part of the water column between bin numbers 50 and 65 where the magnitude
427of the backscattered raw return signal reaches maximum values. This range encompasses the
428immobile bed, the assumed layers of rolling/sliding and saltating bedload, and part of the
429clear water layer. Variations in the elevation of the surface of the immobile bed level are
430clearly illustrated by the temporal evolution of the location where the maximum magnitude of
431the raw return signal occurs. The bed level aggraded in the beginning of the test and reached
432a maximum level after approximately 60 s. The bed level subsequently gradually lowered and
433reached a quasi-constant level after approximately 165 s. Periods with quasi-constant
434characteristics are first identified and isolated in each experiment (see Table 2 and detailed
435Tables in the supporting information). For the Q1000L experiment shown in Figure 5, for
436example, 5 periods of quasi-constant conditions are identified. The data analysis procedure of
437the ADV measurements is performed separately for each of these periods. For each period

438of quasi-constant conditions the elevation of the surface of the immobile bed, the layer of
439saltating bedload, the layer of rolling and sliding bedload, and the layer of sediment-free clear
440water are defined based the data analysis procedures described above. These layers are
441indicated in all relevant figures.

442

[Figure 5]

443**Digital videography**

444A Basler A311f high-speed digital video camera was used to record images of the mobile bed
445through the sidewall of the flume (Figure 1c). The images gave a distorted picture of the bed
446(due to perspective) but were centred on the ADVP sample volume in the centre of the flume,
447with a 0.122 m centreline longitudinal by 0.155 m transverse field of view. The images had
448656x300 resolution, thus pixel size was approximately 0.0002x0.0005 m. The videography
449maps the three-dimensional sediment motion on a horizontal plane, which is complementary
450to the resolution in a vertical water column provided by the ADVP. Image exposure time was
451300 μ s, and sampling rate was 111 Hz. Computer clock times were used to synchronize image
452acquisition with ADVP data collection. Digital video images were orthorectified using a
453projective transformation (Beutelspacher et al. 1999). Due to limitations in computer storage
454and data transfer, digital videos with high temporal resolution could only be recorded for
455maximum 10 seconds. During the 10-minute ADVP data collection, 10-second digital videos
456were collected once every minute (Figure 5). The cumulative duration of the digital videos of
457more than 110 seconds is long enough to obtain reliable estimates of the velocities of the
458bedload particles. Two complementary image treatment algorithms were used.

459 In order to estimate the velocity of sediment particles, the robust open-source particle
460tracking velocimetry (PTV) algorithm *PolyParticleTracker* was used (Rogers et al. 2007).
461This algorithm is able to estimate the position and track several objects through frames with a

462sub-pixel resolution. The algorithm was specifically developed for tracking bright objects
463over a complex background. The particle instantaneous velocities are then estimated by time
464differentiation of the particle positions. Erroneous trajectories were filtered with techniques
465commonly used in Particle Image Velocimetry. First, a maximum acceleration criterion of 40
466 m s^{-2} was defined for individual particles. Then, the angle between two successive velocity
467vectors was limited to 90° . Particles are often found with velocities close to zero while
468bouncing on the bed. In order to avoid sampling of these quasi-immobile bed particles that
469only marginally contribute to the sediment flux, a minimum velocity threshold of 0.04 m s^{-1}
470was adopted. Full trajectories of particles, from entrainment to deposition were not always
471recovered by the algorithm, mainly due to the presence of the noisy background composed of
472resting particles. Moreover, not all of the moving particles were systematically detected. It
473can be expected that especially the saltating bedload with relatively small grain size and
474relatively high velocities was undersampled. Enough particle trajectories were correctly
475recovered to provide a good estimate of the distribution functions of the sediment velocities
476and the time-averaged velocity of the moving sediment particles. These quantities will be
477shown and discussed in the section “Simultaneous videography”.

478 An instantaneous spatio-temporal quantification of the bedload layer velocities was,
479however, not possible from the trajectories obtained with the PTV method, since not all of the
480moving particles were systematically detected by the automated algorithm and since full
481trajectories from entrainment to deposition were not always recovered. In order to estimate
482bedload velocity time series in the ADV sample volume, a complementary analysis of the
483digital video images was performed with the Optical Flow algorithm (Horn and Schunck
4841981). This algorithm remedies the small sample limitation of the particle tracking
485algorithm by computing for each pair of frames a dense 2D velocity field that reflects the

486local apparent motion in the image. The algorithm assumes that the intensity value $I(x,y,t)$ of
487each pixel follows a simple advection equation :

$$488 \quad \frac{\partial I}{\partial t} + u \frac{\partial I}{\partial x} + v \frac{\partial I}{\partial y} = \varepsilon \quad (5)$$

489where the problem unknowns are the velocity components $u(x,y,t)$ and $v(x,y,t)$ along the x and
490 y axes. The partial derivatives of I can be estimated directly from the video stream: $\partial I/\partial t$ is
491the temporal change in pixel intensity, and $\partial I/\partial x$ and $\partial I/\partial y$ are the spatial gradients in pixel
492intensity. The Optical Flow method determines the velocity field (u,v) that minimize ε .
493Intuitively, the apparent motion of an object is better appreciated by the human eye if it
494contains high intensity gradients (border contrasts for instance). On the contrary, the motion
495of objects with low contrast is difficult to estimate by the human eye. This is similar for the
496Optical Flow method, which will perform better when $\partial I/\partial x$ and $\partial I/\partial y$ are larger. In case these
497spatial gradients equal zero, the velocity field (u,v) is not uniquely determined by Equation
498(5) and the problem is ill-posed. In this case, an additional constraint (also called a regularizer
499Horn and Schunck 1981) needs to be imposed, usually based on the continuity of the velocity
500field. The efficiency of this technique relies thus on the presence of strong intensity gradients,
501as those frequently observed at object edge contours. The Optical Flow algorithm can be
502expected to be especially appropriate for the largest bedload particles that roll and slide on the
503immobile bed, because these particles form well distinguishable contours in the digital
504images that yield large gradients $\partial I/\partial x$ and $\partial I/\partial y$. Faster and smaller bedload particles can be
505expected to be undersampled due to their weaker intensity gradients. This algorithm has been
506successfully applied in numerous applications, including flow reconstruction from Particle
507Image Velocimetry techniques (Ruhnau et al. 2005, Heitz et al. 2008), but it has yet rarely
508been applied to the estimation of sediment motion (Spies et al. 1999, Klar et al. 2004). Here,
509the Optical Flow algorithm has been applied to investigate the time-resolved velocity of the

510bedload particles inside the ADVP sample volume. The particle velocities have been
511estimated from the digital video images with the open access Matlab implementation of the
512Lukas-Kanade Method (Lucas and Kanade, 1981) by Stefan M. Karlsson and Josef Bigun
513and available at <http://www.mathworks.com/matlabcentral/fileexchange/40968>. In order to
514improve the accuracy and to reduce noise, the velocity field was averaged on a 70x70 grid
515overlapping the original 656x300 pixels images. The local sediment velocity spatially-
516averaged within the footprint of the ADVP's measuring beam at the bed was then obtained by
517averaging the 70x70 Optical Flow velocity field using a Gaussian kernel centred on the
518volume. It is worth noting that this spatial average also includes areas of zero velocity
519associated with immobile particles, and thus reflects the average bed velocity. This is
520different from the sediment velocities estimated with the PTV algorithm, which only
521considers moving sediment particles. It is similar, however, to the velocities measured by the
522ADVP in the bin containing the surface of the immobile bed (cf. section "ADVP
523configuration and data analysis procedures"). The temporal fluctuations of this locally
524spatially averaged velocity will be shown and discussed in the section "Simultaneous
525videography".

526RESULTS

527Signature of the raw signals recorded by the ADVP

528Most commercial ADVP systems only provide as output the quasi-instantaneous Doppler
529frequencies or velocities sampled at PRF/NPP. The ADVP used in the present investigation
530also provides the backscattered raw return signals recorded by the receivers, I and Q , sampled
531at PRF. This is a major advantage, as it allows analysing the raw signals for the presence of a
532footprint of bedload sediment transport. This analysis will be illustrated for the Q795L
533experiment, where the bed level remained stable during the entire 624 s of continuous
534measurements.

535 First, the time-averaged magnitude of the backscattered raw return signal, $I^2 = 0.25$
536 $(I_1^2 + I_2^2 + I_3^2 + I_4^2)$ is considered (Figure 2). The magnitude of the backscattered signal relates to
537 the concentration of the sediment particles, because sediment particles backscatter
538 considerably more acoustic energy than micro air-bubbles in the water column above
539 (Hurther et al. 2011). The magnitude of the return signal decreases with distance upwards
540 from the immobile bed level, which complies with the expectation that sediment
541 concentration decreases with distance from the immobile bed. We hypothesize that the bins
542 with considerably increased magnitude of the return signal correspond to the layer of rolling
543 and sliding bedload sediment, and that bins characterized by the base level of acoustic
544 backscatter magnitude correspond to clear water flow. Bins in between the rolling and sliding
545 bedload transport layer and the clear water flow layer are assumed to correspond to saltating
546 bedload.

547 Second, the signature of the time-series of the I signal is investigated in bins near the
548 bed. Figure 6 focuses on a 0.2 s time-series sampled at PRF = 1000 Hz in the bin containing
549 the immobile bed and the three overlaying bins. According to the definition (Equation (2)),
550 the I signal produced by a moving acoustic scattering source should fluctuate around a zero
551 value. Figure 6 clearly shows an offset in the time-averaged value of the I signal, especially
552 for bins 57 and 58. This offset is due to imprecision in the analog demodulation of the
553 measured signal. In order to prevent biased estimates, it is important to remove this offset
554 from the signal before estimating the Doppler frequency according to Equation (4). The
555 increase in magnitude of the raw return signal towards the bed observed in Figure 2 can be
556 recognized in the increasing amplitude of the I fluctuations towards the bed in Figure 6. The I
557 signal in bin 55 shows oscillations with a frequency and amplitude that varies in time, as can
558 be expected for flow velocities in clear water. According to Hurther and Thorne (2011) and
559 Naqshband et al. (2014b), the zero velocity and highest sediment concentration at the

560 immobile bed surface, estimated within bin 58, should in theory correspond to a constant I
561 value of high amplitude with negligible variance. Figure 6 shows that the measured amplitude
562 is not always constant, but that sequences of fluctuating voltage occur. These sequences
563 represent the intermittent passage of bedload particles that roll and slide on the immobile bed
564 (cf. section “ADVP configuration and data analysis procedures” and Figure 4).

565

[Figure 6]

566 Third, the power spectral densities of the I signals simultaneously recorded by the
567 four receivers are investigated. According to the theory outlined in the introduction, the
568 frequency of the fluctuating I signal is proportional to the velocity of the acoustic scatterers.
569 Hence, the power spectral density of the I signal represents the turbulent fluctuations of the
570 velocity of the acoustic scatterers (Traykovski 1998, his appendix A). Figure 7 shows these
571 power spectral densities in the bins corresponding to the estimated layers of rolling and
572 sliding bedload, saltating bedload, and clear water. For the bin in clear water, these spectral
573 densities are near Gaussian, as expected for turbulent velocity fluctuations. The peak value
574 corresponds to a velocity of about 0.4 m s^{-1} , which compares favourably with the time-
575 averaged velocity estimated using the pulse-pair algorithm (Equation 4, Figure 3b). The
576 lower and higher values represent the turbulent velocity fluctuations. Interestingly, however,
577 the power spectral density is left-skewed in the bin that is assumed to correspond to the
578 rolling and sliding bedload layer, which is more consistent with observations of bedload
579 particle velocities (Drake et al. 1988; Rennie and Millar 2007; Lajeunesse et al. 2010; Furbish
580 et al. 2012). In the assumed layer of saltating bedload, the spectral densities look like a
581 combination of a Gaussian and a left-skewed profile.

582

[Figure 7]

583 Fourth, the signature of the time-series of the velocity is investigated in bins near the
584bed (Figure 8). Velocity fluctuations in the first two bins of the assumed clear water layer
585(bins 54 and 55) are similar and represent turbulent coherent structures. The velocity
586fluctuations in bin 56, corresponding to the assumed layer of saltating bedload, seem to be
587coherent with the fluctuations in the clear water layer, but the amplitude of the velocities is
588considerably reduced. The velocities in the assumed layer of rolling and sliding bedload (bin
58957) show less coherence with the turbulent coherent structures in the clear water above. The
590velocity is considerably smaller in bin 58 containing the immobile bed surface. The non-zero
591velocities represent the intermittent passage of bedload particles that roll and slide on the
592immobile bed (cf. section “ADVP configuration and data analysis procedures” and Figure 4).

593 [Figure 8]

594 A similar analysis of the characteristics of the backscattered raw return signal I (Figures
5952, 6, 7) and the time-series of the velocities (Figure 8) has been performed for all
596experiments. This analysis revealed a clear footprint of the bedload sediment transport in the
597raw return signals, which indicates that the moving bedload sediment grains are the main
598scattering sources. Because the ADVP measures the velocity of the scattering sources, this
599analysis provides a first indication that the velocities measured by the ADVP correspond to
600the velocities of the moving sediment particles. Moreover, this analysis corroborated the
601identification based on the profile of the time-averaged velocity (Figure 3b) of the bin
602containing the immobile-bed surface, the layer of rolling and sliding bedload, and the layer of
603saltating bedload.

604**Simultaneous ADVP measurements and videography**

605Figure 9 shows the results for the time-averaged velocities in the main series of experiments.
606All relevant information is provided in Table 2 for the experiments with low acoustic power

607and in Table S1 of the supporting information for the experiments with high acoustic power.
608The total duration of each experiment has first been divided into periods with quasi-constant
609conditions. The reference z-level has been taken as the lowest level of the immobile-bed
610surface during the total duration of each experiment. The rise of the immobile bed level
611during the passage of a dune in the Q630L experiment, for example, is visible in the shift to
612right of the measured velocity profiles in Figure 9a. Similarly, the important variations in the
613immobile bed level due the break up of the armour layer in the Q1000L experiment are
614clearly visible in Figure 9e.

615 [Figure 9]

616 For each of the periods with quasi-constant conditions, the vertical profile of
617streamwise velocity measured in water column bins within the sensitivity range of the ADVP
618(beyond gate 37) fit the log-law very well (Figure 9). However, measured velocities in the
619near-bed bins was systematically less than expected from the log-law.

620 In the near-bed zone, the bin containing the immobile-bed surface and the layers of
621rolling and sliding bedload, saltating bedload, and clear water have been identified from the
622time-averaged velocity profile and the profile of the magnitude of the backscattered raw
623return signal as described in the section “ADVP configuration and data analysis procedures”.
624The identification of these different layers was confirmed by the analysis of the backscattered
625raw return signal I and the time-series of the velocities as described in the section “Signature
626of the raw signals recorded by the ADVP”.

627 The gray shaded areas in Figure 9 represent the distribution functions of the sediment
628velocities based on the PTV treatment of the eleven sequences of videography in each
629experiment (e.g., periods marked by red lines in Figure 5). The average particle velocity
630computed from these distribution functions, also indicated in the figure, agrees well with the

631ADVP estimation of the dominant bedload velocity, which occurs at the elevation where the
632slip velocity is maximum (cf. section “ADVP configuration and data analysis procedures”).
633The relative and absolute differences between the average particle velocity estimated from
634ADVP and videography in each experiments are $21 \% \pm 9\%$ and $0.0275 \text{ m s}^{-1} \pm 0.0125 \text{ m s}^{-1}$,
635respectively. This absolute difference is much smaller than the velocity variation within one
636bin of the ADVP measurements (Figure 9).

637 The average bedload velocity in the Q795L experiment is similar to that in the Q630L
638experiment, which can be attributed to the armouring of the bed. The average bedload
639velocity in the Q1000L experiment is substantially higher. The highest velocities of bedload
640particles observed in the video images (highest velocities in the gray distribution functions)
641were only slightly smaller than the velocity measured with the ADVP at the top of the non-
642logarithmic flow layer near the bed (Figure 9). This observation supports the hypothesis that
643these fastest moving particles were saltating bedload particles that had less slip velocity than
644rolling and sliding bedload particles. The shape of the distribution functions based on the
645videography (Figure 9) resemble the shape of the power spectral density distributions of the
646velocities measured with the ADVP in the bedload layer (Figure 7), further suggesting that
647the latter represent the velocity of the bedload sediment particles.

648 For the three investigated conditions shown in Figure 9, each experiment with low
649acoustic power was immediately followed by an experiment with high acoustic power (Figure
6502). The latter corresponds to the standard ADVP configuration for optimal flow
651measurements in the body of the water column, but may lead to magnitudes of the
652backscattered raw return signal I that are frequently out of the recording range of the
653receivers near the bed. The former corresponds to the ADVP configuration optimized for
654measurements near the bed. A better resolution of the sediment velocity would be expected
655with low acoustic power and a better resolution of the flow with high acoustic power.

656Differences between results from experiments with low and high acoustic power were found
657to be insignificant and within the experimental uncertainty (Figure 9). However, for the Q795
658experiments, only about 10 % of the raw $I(t)$ signal had a magnitude outside the receivers'
659recording range in the bin containing the surface of the immobile bed in the experiment with
660low acoustic power (Figure 2; Figure 6d), whereas 36% was out-of-range in the experiment
661with high acoustic power (Figure 2). These results demonstrate the robustness of the pulse-
662pair algorithm (Equation 4), which provides accurate estimations of the average velocity even
663in the presence of a non-negligible number of out-of-range values of I and Q . An important
664conclusion from this result is that measurements of the bedload sediment velocities can be
665performed with the standard configuration of the ADVP.

666

[Figure 10]

667 Figure 10 shows time series of the velocities in the main series of experiments with low
668acoustic power. It compares the quasi-instantaneous velocities spatially averaged within the
669ADVP measurement volume estimated with the Optical Flow algorithm to those measured
670with the ADVP in the bin containing the surface of the immobile bed and the bin just above
671(Table 2), where the rolling and sliding bedload sediment transport occurs. As explained
672before, the upper part of the bin containing the surface of the immobile bed is situated in the
673flow where bedload sediment particles roll and slide on the immobile bed (Figure 4), whence
674the ADVP measures in that bin a non-zero velocity. As also explained before, both the ADVP
675measurement in the bin containing the surface of the immobile bed, and the Optical Flow
676algorithm provide an average sediment velocity that includes areas of zero velocity associated
677with immobile particles. This explains why they provide velocities that are substantially
678lower than those estimated with the PTV algorithm, which only considers moving sediment
679particles in the water column (Figure 9).

680 For the sake of clarity, only two 10 s sequences of videography are shown for each
681 experiment. In the Q630L and Q795L experiments, both the magnitude and the time series of
682 the quasi-instantaneous velocities estimated from the videography with the Optical Flow
683 algorithm agree very well with those measured by the ADVP in the bin containing the
684 immobile-bed surface (Figures 10a and 10b), indicating that most of the bedload sediment
685 transport occurred in the form of rolling and sliding particles within the bin containing the
686 immobile-bed surface. This complies with the observation that only partial transport of
687 sediment occurred in these experiments (Table 1), and that the largest particles moving were
688 smaller than the ADVP's bin size. In the Q1000L experiment, the temporal evolutions of the
689 velocities estimated from the videography and measured with the ADVP are clearly related,
690 but the velocities estimated with the Optical Flow algorithm are generally smaller than those
691 measured with the ADVP. In this experiment, generalized intense sediment transport occurred
692 (Table 1), and the largest particles moving were larger than the ADVP's bin size. The layer of
693 rolling and sliding bedload particles was at least two bins thick, and overlaid by a layer of
694 smaller and faster moving saltating bedload particles of at least three bins thick (Figures 9e
695 and 9f) The underestimation of the bedload velocities in the Q1000L experiment by the
696 Optical Flow algorithm is tentatively attributed to the fact that the algorithm only resolves the
697 velocity of the largest and slowest bedload particles, whereas the ADVP resolves the velocity
698 of all particles.

699 These results are further substantiated by the cross-correlations between the
700 fluctuations of velocities measured with the ADVP in the bin containing the surface of the
701 immobile bed and estimated with the Optical Flow algorithm. These cross-correlations are
702 defined as:

$$C = \frac{\overline{u_{ADVP} u_{OF}}}{\sqrt{\overline{u_{ADVP}^2}} \sqrt{\overline{u_{OF}^2}}} \quad (6)$$

703

704 where the prime denotes the fluctuating component of the velocity time-series and the
705 overbar denotes time-averaging. The cross-correlation for the Q1000L experiment are
706 relatively low at $C=0.22\pm 0.04$, which complies with the important deviations between the
707 time-series measured by ADV and Optical Flow (Figure 10c). The cross-correlations for the
708 Q630L and Q795L experiments are considerably higher at $C=0.41\pm 0.04$ and $C=0.74\pm 0.04$,
709 respectively. These values further indicate that the ADV also resolves the details of the
710 temporal fluctuations of bedload particle velocities.

711 Comparison to semi-theoretical formulae based on previous results

712 Figure 11 summarizes results from all experiments, including the second series of
713 experiments with flow depths of 0.14 m and 0.24 m measured with the standard configuration
714 of the ADV with high acoustic power, and without simultaneous videography. All relevant
715 information is provided in tabular form as supporting information. For each of these flow
716 depths, ten different discharges were tested, ranging from conditions without sediment
717 transport to conditions with generalized sediment transport. Figure 11 presents the bedload
718 velocity and layer thicknesses measured with the ADV as a function of the shear velocity u_* .
719 In straight uniform open-channel flows, Nezu and Nakagawa (1993) have proposed a semi-
720 theoretical logarithmic profile for the streamwise velocity, exponential profile for the
721 turbulent kinetic energy, and linear profile for the streamwise-vertical turbulent shear stress,
722 which all scale with the shear velocity. Fitting of the measured vertical profiles to these semi-
723 theoretical similarity solutions provides three estimates of u_* . The average of these three
724 estimates is used on the abscissa in Figure 11. Each of the experiments of the second series
725 was also divided into periods of quasi-constant conditions. Because differences between
726 different periods were relatively small, only one average result is reported in Figure 11 for
727 each experiment.

728

[Figure 11]

729 Figure 11a reports the velocity of the bed load particles estimated from the ADVP
730 measurements. For the main series of experiments, bedload velocity estimated from the
731 videography with the PTV algorithm is also shown. For u_* smaller than 0.02 m s^{-1} , the bed is
732 stable and no bedload sediment transport occurs. Note that $u_{*,cr} = 0.02 \text{ m s}^{-1}$ corresponds to
733 the critical shear velocity for the initiation of sediment transport for d_{50} based on the Shields
734 criterion (Shields 1936). When bedload transport occurs, the bedload velocity increases with
735 increasing shear velocity, in line with results reported in literature. According to Lajeunesse
736 et al. (2010, their equations 26 and 27), the average velocity of bedload particles, $v_{bedload}$, can
737 be written as:

$$738 \quad v_{bedload} = a(u_* - u_{*,cr}) + 0.11v_{settling} \quad (7)$$

739 where u_* and $u_{*,cr}$ are the shear velocity and the critical shear velocity for the initiation of
740 bedload transport, respectively, and $v_{settling}$ is the characteristic settling velocity of the
741 sediment. As mentioned above, the critical shear velocity for d_{50} is 0.02 m s^{-1} . According to
742 Brown and Lawler (2003) the settling velocity for d_{50} is 0.118 m s^{-1} . Different values are
743 reported in literature for the coefficient a . Based on experimental observations of sediment
744 moving above a mobile bed, Lajeunesse et al. (2010) reported a value of 4.4 ± 0.2 whereas
745 Fernandez-Luque and Van Beek (1976) reported a value of 13.2 ± 0.6 . The latter value was
746 also reported by Abbott and Francis (1977) and Lee and Hsu (1994) for a single grain particle
747 entrained above a rigid rough bed. The a value proposed by Lajeunesse et al. (2010) was
748 based on experiments with sediment diameters of $d_{50} = 0.00115 \text{ m}$, 0.00224 m and 0.0055 m ,
749 and Shields parameters in the range from 0.006 to 0.24. Fernandez-Luque and Van Beek
750 (1976) performed experiments with sediment diameters of $d_m = 0.0009 \text{ m}$, 0.0018 m , and
751 0.0033 m , and ratios of the Shields parameter to the critical Shields parameter for the
752 initiation of motion of 1.1 to 2.7. These experimental conditions are comparable to those in
753 the experiments reported in the present paper. The bedload velocity according to equation 7

754for both values of $a = 4.4$ and 13.2 envelopes all data from the here reported experiments
755(Figure 11a).

756 Figure 11b reports the thickness of the layer of rolling and sliding bedload (defined in
757the section “ADVP configuration and data analysis procedures“ and indicated in Figure 9)
758estimated from the ADVP measurements, which increases as expected with increasing shear
759velocity. The resolution of the bedload layer thickness is obviously limited by the size of the
760ADVP measuring bins of 0.004 m. The estimated bedload layer thickness increases from
761about 1 bin (0.004 m) at low transport to about 2 bins at high transport (0.008 m). Based on
762the solution of the equations of motion for a solitary particle, van Rijn (1984, Equation 10)
763proposed the following equation for the bedload layer thickness:

$$764 \quad \text{thickness} = 0.3 d \left[d \frac{(\rho_s/\rho - 1) g}{\nu^2} \right]^{1/3} (u_*^2/u_{*c}^2 - 1)^{1/2} \quad (8)$$

765where d is a characteristic diameter of the bedload sediments, taken as d_{50} by van Rijn (1984),
766 ρ_s and ρ are the densities of the sediment and the water, respectively, g is the gravitational
767acceleration and ν is the kinematic viscosity of the water. Van Rijn (1984) calibrated this
768equation based on experiments with a uniform sediment diameter of $d = 0.0018$ m and a shear
769velocity of 0.04 m s⁻¹. These parameters are in the same range as in the experiments reported
770herein. All data on the bedload layer thickness estimated from the ADVP measurements in the
771present experiments are constrained by two curves, corresponding to predictions based on
772Equation 8 for bedload sediment diameters of $d = d_{50} = 0.0008$ m and $d = 0.0015$ m. Hence,
773the ADVP estimates of the bedload layer thickness comply with the equation and underlying
774experiments of van Rijn (1984).

775 It is noteworthy that results for the velocities and thicknesses are quite similar for
776experiments Q630 and Q795 in the main series of experiments, and strongly increase from

777Q795 to Q1000. This behaviour can be attributed to the gradual formation of the armour layer
778in Q630, which limits bedload transport in Q795, and the break up of the armour layer in
779Q1000.

780**Comparison of standard ADVP configuration and ADVP configuration optimized for** 781**bedload measurements**

782 Both for the sediment velocity in the bedload layer, and the thickness of the dominant
783bedload layer, results of the experiments with a flow depth of 0.24 m in the second series
784with standard ADVP configuration (Table S2 of the supporting information) agree well with
785results in the main series with ADVP configuration optimized for bedload measurements
786(Table 2). Experiments with similar hydraulic conditions are compared (Q630L vs. Q605H,
787Q795L vs. Q794H and Q795H, and Q1000L vs. Q897H). The relative and absolute
788differences between the average particle velocity estimated with standard and optimized
789ADVP configurations are $20 \% \pm 8\%$ and $0.032 \text{ m s}^{-1} \pm 0.025 \text{ m s}^{-1}$, respectively. This
790absolute difference is much smaller than the velocity variation within one bin (Figure 9).
791Both ADVP configurations provided identical estimations of the thickness of the dominant
792bedload layer. This confirms that the standard ADVP configuration provides reliable
793estimations of the bedload characteristics. It is noteworthy that results for the velocities and
794thicknesses are quite similar for experiments Q630 and Q795 in the main series of
795experiments, and strongly increase from Q795 to Q1000. This behaviour can be attributed to
796the gradual formation of the armour layer in Q630, which limits bedload transport in Q795,
797and the break up of the armour layer in Q1000.

798**DISCUSSION AND CONCLUSIONS**

799 Previous experiments have indicated that near-bed velocities can deviate from the
800logarithmic profile due to beam geometry effects, i.e. contamination of the near-bed bins by

801high intensity scatter from the immobile bed (Hay et al. 20121), and due to the presence of
802bedload sediment transport (Naqshband et al. 2014b). The ellipses of equal acoustic travel
803time for the near-bed bins have been drawn in Figures 1a and 1b for the ADVP configurations
804adopted in the here reported experiments. These purely geometrical considerations indicate a
805potential contamination zone due to beam geometry effects of approximately 0.01 m. This is
806a conservative estimation, however, which does not take into account that the acoustic power
807is maximal in the centre of the insonified beam and decays in a Gaussian way towards its
808edges. In all experiments without sediment transport reported in this paper, the ADVP
809resolved the law of the wall logarithmic velocity profile, including in the first bin above the
810immobile bed (Figure 3a). This indicates that the contamination zone due to beam geometry
811effects is smaller than 0.004 m. On the contrary, in all experiments with bedload sediment
812transport reported in this paper, velocities in the near-bed region where bedload sediment
813transport occurs were systematically smaller than expected from the logarithmic law of the
814wall (Figure 3a,b and Figure 9), similar to observations by Naqshband et al. (2014b). The
815deviating velocities occurred in a layer of approximately 0.004 m to 0.02 m from the
816immobile bed (Figure 3 and Figure 9). These observations indicate that the velocity deficit in
817the near-bed region is essentially related to the transport of bedload in the reported
818experiments.

819 Results from all three strategies corroborate the main hypothesis of the present paper
820that the ADVP does measure sediment velocities, also in the near-bed layer where bedload
821transport occurs. First, the backscattered raw return signals $I(t)$ recorded by the ADVP's
822receivers reveal a clear footprint of the bedload sediment particles. The magnitude of $I(t)$ in
823the bins where bedload sediment transport occurs clearly exceeds that of bins above in the
824clear water flow (Figures 2 and 6) , which is due to the fact that sediment particles
825backscatter considerably more acoustic energy than micro air-bubbles in the clear water

826(Hurther et al. 2011). Thus, the sediment particles are the main scattering sources in the
827insonified water column, and it is therefore their velocity that is measured by the ADV. P.
828Spectra of the $I(t)$ signals are near-Gaussian in the clear water and left-skewed near the bed
829where bedload sediment transport occurs. The latter distribution is characteristic for bedload
830sediment transport (Figure 7), in agreement with recent findings (Drake et al. 1988, Rennie
831and Millar 2007, Lajeunesse et al. 2010, Furbish et al. 2012). Second, results from the
832simultaneous videography of the bedload sediment transport are in good agreement with
833ADV results. Time-averaged velocities measured with the ADV in the layer of rolling and
834sliding bedload transport agree well with those estimated from the digital video images of the
835moving sediment with a particle tracking algorithm (Figure 9). Moreover, velocity time series
836(mean and fluctuating components) measured with the ADV in the bin containing the
837immobile-bed surface agree well with the time series of the average bed velocity estimated
838with the Optical Flow algorithm (Figure 10). Third, ADV based estimates of the bedload
839velocities and thickness of the bedload layer are in agreement with semi-theoretical formulae
840based on previous experiments proposed by Lajeunesse et al. (2010) and van Rijn (1984),
841respectively, for a broad range of hydraulic conditions (Figure 11).

842 The ADV configuration optimized for bedload measurements only marginally
843performs better than the standard configuration for flow measurements, which also provides
844satisfactory estimates of the sediment velocity and transport layer thickness.

845 These findings corroborate the hypothesis of Hurther et al. (2011) and Naqshband et al.
846(2014b) that the ADV can measure the time-averaged velocity of bedload particles, and the
847hypothesis of Naqshband et al. (2014a) that it also measures the temporal fluctuations of the
848particle velocities. The shear velocities in the reported experiments were comparable to those
849in the experiments of Naqshband et al. (2014a,b), but their sediment size was about 10 times
850smaller, leading to Shields numbers that were about 10 times higher, and resulting in more

851intense bedload transport and significant suspended load transport. Both the present study and
852Naqshband et al. (2014a,b) used a similar ADVP with carrier frequency $f_0 = 1$ MHz, resulting
853in a wavelength of the emitted acoustic pulses of about $\lambda = c/f_0 = 0.0015$ m. The sediment
854particles were smaller than this wavelength in Naqshband's experiment, leading to Rayleigh
855backscattering of the acoustic pulse. The particles were larger than this wavelength in our
856experiments, leading to geometric scattering. These results indicate that the ADVP is able to
857measure turbulent bedload velocities and the bedload layer thickness for a broad range of
858sediment diameters and different regimes of scattering.

859 These results confirm that ACVPs (Hurther et al. 2011), which integrate an ADVP with
860an Acoustic Backscatter System (ABS), are able to measure turbulent sediment fluxes
861according to Equation (1). The ABS ability to measure sediment concentration in the entire
862water column, including the bedload layer, has been demonstrated (Naqshband et al. 2014b).
863When sediment transport occurs, the ADVP provides unbiased measurements of the sediment
864velocity u_s , even in the near-bed layer where bedload sediment transport occurs. Velocities of
865bedload sediment will be smaller than velocities of the surrounding water, whereas velocities
866of suspended load sediment will be about equal to velocities of the surrounding water. When
867no sediment transport occurs, the ADVP measures the velocity of the clear water flow. The
868presence or non-presence of sediment in the water column is indicated by the ABS
869measurements of concentration. The position of the surface of the immobile bed can
870independently be estimated from the ADVP measurements as in the present paper, and from
871the ABS measurements as done by Hurther et al. (2011).

872 The present paper has proposed straightforward criteria based on the shape of the
873velocity profile to identify the layers of rolling and sliding bedload, saltating bedload, and
874suspended load or clear water (Figures 3 and 9). As a complementary approach, Hurther et al.
875(2011) identified the suspended load layer based on characteristics of the concentration

876 profile measured with ABS, and defined the bedload layer as the intermediate layer between
877 the immobile bed and the suspended load layer. The identification of these different layers is
878 mainly important for comparison to commonly used formulae for bedload and suspended
879 load transport. It is of minor importance in practical applications, however, because the river
880 morphology is mainly determined by the total sediment flux estimated according to Equation
881 (1).

882 The reported ADVP bedload results are sensitive to vertical resolution of the ADVP
883 system. The bin size in the reported experiments was 0.004 m, which is the minimum bin size
884 of the applied ADVP. Uncertainty in the determination of the levels of the immobile-bed
885 surface, the layer of rolling and sliding bedload, and the layer of saltating bedload is about
886 half a bin. In this case, the uncertainty of about 0.002 m in the vertical elevation is
887 comparable to the mean diameter of the sediment ($d_m = 0.0023$ m). Moreover, the near-bed
888 velocities change considerably within one bin (cf. Figure 9). Using interpolated estimates of
889 these levels corresponding to half a bin (included in tabular form in Table 2 for the main
890 series of experiments with low acoustic power and in the supporting information for the other
891 experiments) considerably reduces discrepancies between velocities measured with ADVP
892 and estimated from the digital video images, as well as the scatter in Figure 11 (which is not
893 based on half-bin interpolations). These observations highlight the importance of an optimal
894 choice of the ADVP parameters, and especially the bin size, which should be small compared
895 to the thickness of the bedload layer. Naqshband et al. (2014a) adopted a bin size of 0.003 m
896 in their investigation of sediment fluxes over equilibrium dunes, which was the minimum bin
897 size of their ADVP, whereas the broadband multifrequency ADVP developed by Hay et al.
898 (2012 a,b,c) is capable of a bin size of 0.0009 m.

899 A major advantage of ADVP's is their versatility, and the possibility to optimize their
900 configuration for particular applications. The bin size, for example, is constrained by the

$$V_{\max} = PRF \frac{C}{4 f_0}$$

901wavelength of the emitted acoustic pulse, $\lambda = c/f_0$, and can be reduced by increasing the
 902carrier frequency f_0 , bearing in mind that the maximum unambiguously measureable velocity
 903is inversely proportional to f_0 (Pinkel 1980).

904 (9)

905PRF is also related to the maximum profiling range D_{max} , which represents the longest travel
 906path of the acoustic pulse between emitter and receiver in the measured water column:

907
$$D_{max} = \frac{c}{2PRF} \tag{10}$$

908In the here applied ADVP configuration, D_{max} is slightly larger than twice the maximum
 909height of the investigated water column. Combining the constraints in equations (9) and (10)
 910leads to the well-known range-velocity ambiguity relations in pulse-coherent Doppler
 911systems (Pinkel 1980):

912
$$4V_{max} \frac{f_0}{c} < PRF < \frac{c}{D_{max}} \quad \text{and} \quad V_{max} D_{max} = \frac{c^2}{4f_0} \tag{11}$$

913These relations show that pulse coherent systems must trade off the bin size, maximum
 914observable velocities and maximum range of profiling, depending on operating frequency. If
 915operating frequency is increased to reduce bin size, then PRF could be increased to maintain
 916the same maximum measurable velocity (Equation 9). However, the profiling range would be
 917reduced (Equation 10). This is not a major drawback in sediment transport applications,
 918where the main region of interest is located in the vicinity of the bed. The ADVP acoustic
 919operating frequency can be optimized based on the transport velocity and thickness of the
 920bedload layer as predicted, for example, by means of Equations (7) and (8). It is worth noting
 921that these principles underlying the optimal choice of the operating frequency, PRF and
 922profiling range of the ADVP configuration are identical in measurements of turbulent flow

923and measurements of sediment transport, although high sediment concentration may impede
924use of higher operating frequencies due to increased acoustic attenuation.

925 The ADVP and the data treatment procedure outlined in the present paper can be
926applied for sediment transport investigations in the laboratory and in the field. The standard
927set-up for field investigations would involve placing the ADVP transducers immersed in the
928flowing water about $O(1\text{m})$ above the surface of the immobile bed, in order to focus on the
929near-bed region where sediment transport occurs. The ADVP could be mounted on a standard
930platform as commonly used in field investigations in river and coastal applications. Such a
931set-up would also be appropriate to validate the in-field ADCP technique for measuring the
932apparent bedload velocity developed by Rennie et al. (2002), Rennie and Church (2010) and
933Williams et al. (2015).

934 The demonstrated capability of the ADCP (which integrate ADVP and ABS) to measure
935sediment fluxes, including bedload fluxes has important implications, because no reliable
936technique is at present available to measure sediment fluxes. The results broaden the
937application range of ADCP in laboratory and field investigations, and should lead to
938enhanced insight in the dynamics of sediment transport and morphodynamic processes.
939Follow-up studies are required in bespoke laboratory settings with an optimized simultaneous
940deployment of ADVP and high-speed videography, and possibly complementary physical
941sampling, in order to estimate the accuracy and uncertainty in the sediment velocity
942measurements, and to delimit the application range of the ADVP technique.

943

944**Acknowledgements**

945 Blanckaert was partially funded by the Distinguished Visiting Scientist Program of the
946University of Ottawa, grant number 602311. Rennie was partially funded by a Visiting

947 Professor grant from École Polytechnique Fédérale de Lausanne and a Discovery Grant from
948 the Natural Sciences and Engineering Research Council of Canada. We wish to thank
949 uOttawa M.A.Sc. student Saber Ansari for performing the manual particle tracking used to
950 validate the automated particle tracking algorithm. All data can be obtained from Koen
951 Blanckaert (koen.blanckaert@epfl.ch).

952 REFERENCES

953 Abbott, J., and J. Francis (1977), Saltation and suspension trajectories of solid grains in a
954 water stream, *Philos. Trans. R. Soc. London A*, 284, 225–254.

955 Ancy, C., and J. Heyman (2014), A microstructural approach to bed load transport: Mean
956 behaviour and fluctuations of particle transport rates, *J. Fluid Mech.*, 744, 129-168.

957 Beutelspacher, A., and U. Rosenbaum (1998), *Projective Geometry: From Foundations to*
958 *Applications*, Cambridge Univ. Press, Cambridge, UK, ISBN 0-521-48364-6.

959 Blanckaert, K. (2010), Topographic steering, flow recirculation, velocity redistribution,
960 and bed topography in sharp meander bends, *Water Resour. Res.*, 46, W09506,
961 doi:10.1029/2009WR008303.

962 Blanckaert, K., and H. J. de Vriend (2004), Secondary flow in sharp open channel bends, *J.*
963 *Fluid Mech.*, 498, 353–380.

964 Blanckaert, K., and U. Lemmin (2006), Means of noise reduction in acoustic turbulence
965 measurements, *J. Hydraulic Res.*, 44(1), 3-17.

966 Bose, S. K., and S. Dey (2013), Sediment entrainment probability and threshold of sediment
967 suspension: exponential-based approach, *J. Hydr. Eng.*, 139(10), 1099-1106.

968Bricault, M. (2006), Rétrodiffusion acoustique par une suspension en milieu turbulent:
969 application à la mesure de concentration pour l'étude des processus hydrosédimentaires.
970 PhD thesis, Grenoble Institut National Polytechnique.

971Brown, P. P., and D. F. Lawler (2003), Sphere drag and settling velocity revisited. *J.*
972 *Environmental Eng.*, 129(3), 222-231.

973Cellino, M., and W. H. Graf (2000), Experiments on suspension flow in open channels with
974 bedforms, *J. Hydraul. Res.*, 38, 289–298.

975Church, M. (2006), Bed material transport and the morphology of alluvial river channels,
976 *Ann. Rev. Earth and Planetary Sciences*, 34 , 325-354.

977Crawford, A. M., and A. E. Hay (1993), Determining Suspended Sand Size and
978 Concentration from Multifrequency Acoustic Backscatter, *J. Acoustical Soc. Am.*, 94(6),
979 3312-3324.

980Drake, T. G., Shreve, R. L., Dietrich, W. E., Whiting, P. J., and L. B. Leopold (1988), Bedload
981 transport of fine gravel observed by motion-picture photography, *J. Fluid Mech.*, 192, 193-
982 217.

983Ferguson, R. I., Ashmore, P. E., Ashworth, P. J., Paola, C., and K. L. Prestegard (1992),
984 Measurements in a braided river chute and lobe 1. flow pattern, sediment transport, and
985 channel change, *Water Resour. Res.*, 28(7), 1877-1886.

986Fernandez-Luque, R., and R. Van Beek (1976), Erosion and transport of bed-load sediment,
987 *J. Hydraul. Res.*, 14, 127–144.

988Frey, P., Ducottet, C., and J. Jay (2003), Fluctuations of bed load solid discharge and grain
989 size distribution on steep slopes with image analysis, *Exp. Fluids*, 35 (6), 589{597.

990 Furbish, D. J., Roseberry, J. C., and M. W. Schmeeckle (2012), A probabilistic description of
991 the bed load sediment flux: 3. The particle velocity distribution and the diffusive flux, *J.*
992 *Geophys. Res.: Earth Surf.*, 117(3), F03033.

993 Gaeuman, D., and R. B. Jacobson (2006), Acoustic bed velocity and bed load dynamics in a
994 large sand bed river, *J. Geophys. Res.: Earth Surf.*, 111(2), F02005.

995 Guerrero, M., Rütger, N., Szupiany, R., Haun, S., Baranya, S., and F. Latosinski (2016), The
996 Acoustic Properties of Suspended Sediment in Large Rivers: Consequences on ADCP
997 Methods Applicability, *Water-MDPI*, 8(1), Article number 13.

998 Guerrero, M., Szupiany, R. N., and M. L. Amsler (2011), Comparison of acoustic
999 backscattering techniques for suspended sediments investigations, *Flow Meas. Instrum.*,
1000 22, 392-401.

1001 Guerrero, M., Szupiany, R. N., and F. Latosinski (2013), Multi-frequency acoustics for
1002 suspended sediment studies: An application in the Parana River, *J. Hydraul. Res.*, 51, 696-
1003 707.

1004 Hay, A. E., Zedel, L., Cheel, R., and J. Dillon (2012a), Observations of the vertical structure
1005 of turbulent oscillatory boundary layers above fixed roughness beds using a prototype
1006 wideband coherent Doppler profiler: 1. The oscillatory component of the flow, *J.*
1007 *Geophys. Res.: Oceans*, 117(3), C03005, doi:10.1029/2011JC007113.

1008 Hay, A. E., Zedel, L., Cheel, R., and J. Dillon (2012b), Observations of the vertical structure
1009 of turbulent oscillatory boundary layers above fixed roughness using a prototype wideband
1010 coherent Doppler profiler: 2. Turbulence and stress, *J. Geophys. Res.: Oceans*, 117(3),
1011 C03006, doi:10.1029/2011JC007114.

1012 Hay, A. E., Zedel, L., Cheel, R., and J. Dillon (2012c), On the vertical and temporal structure
1013 of flow and stress within the turbulent oscillatory boundary layer above evolving sand
1014 ripples, *Cont. Shelf Res.*, 46(1), 31-49.

1015 Heitz, D., Héas, P., Mémin, E., and, J. Carlier (2008), Dynamic consistent correlation-
1016 variational approach for robust optical flow estimation, *Exp. Fluids*, 45(4), 595-608.

1017 Heyman, J. (2014), A study of the spatio-temporal behaviour of bed load transport rate
1018 fluctuations. PhD thesis no 6256, EPFL, Lausanne, Switzerland.

1019 Heyman, J., Mettra, F., Ma, H. B., and C. Ancey (2013), Statistics of bedload transport over
1020 steep slopes: Separation of time scales and collective motion, *Geophys. Res. Lett.*, 40 (1),
1021 128-133.

1022 Horn, B. K. P., and B. G. Schunck (1981), Determining optical flow. *Artificial Intelligence*,
1023 17(1-3), August 1981 185-203, ISSN 0004-3702, [http://dx.doi.org/10.1016/0004-](http://dx.doi.org/10.1016/0004-3702(81)90024-2)
1024 [3702\(81\)90024-2](http://dx.doi.org/10.1016/0004-3702(81)90024-2).

1025 Hurther, D. (2001), 3-D acoustic Doppler velocimetry and turbulence in open-channel flow.
1026 PhD thesis no 2396, EPFL, Lausanne, Switzerland.

1027 Hurther, D., and U. Lemmin (1998), A constant beamwidth transducer for three-dimensional
1028 Doppler profile measurements in open channel flow, *Meas. Sc. Techn.*, 9(10), 1706-1714.

1029 Hurther, D., and U. Lemmin (2001), A correction method for turbulence measurements with a
1030 3D acoustic Doppler velocity profiler, *J. Atm. Ocean. Techn.*, 18(3), 446-458.

1031 Hurther, D., and U. Lemmin (2008), Improved turbulence profiling with field-adapted
1032 acoustic Doppler velocimeters using a bifrequency Doppler noise suppression method, *J.*
1033 *Atm. Ocean. Techn.*, 25(3), 452-463.

1034 Hurther, D., and P. D. Thorne (2011), Suspension and near-bed load sediment transport
1035 processes above a migrating, sand-rippled bed under shoaling waves, *J. Geophys. Res.:
1036 Oceans*, 116(7), C07001.

1037 Hurther, D., Thorne, P. D., Bricault, M., Lemmin, U., and J. M. Barnoud (2011), A multi-
1038 frequency Acoustic Concentration and Velocity Profiler (ACVP) for boundary layer
1039 measurements of fine-scale flow and sediment transport processes, *Coastal Engineering*,
1040 58(7), 594-605.

1041 Klar, M., Jehle, M., Jähne, B., Detert, M., Jirka, G. H., Köhler, H.-J., and T. Wenka (2004),
1042 Simultaneous 3-D PTV and micro-pressure sensor equipment for flow analysis in a
1043 subsurface gravel layer. *Proc. River Flow 2004*, 703-712. Eds. Greco, Carravetta, and
1044 Della Morte, Taylor & Francis Group, London.

1045 Lajeunesse, E., Malverti, L., and F. Charru (2010), Bed load transport in turbulent flow at the
1046 grain scale: Experiments and modeling, *J. Geophys. Res.: Earth Surf.*, 115(4), F04001.

1047 Latosinski, F., Szupiany, R. N., García, C. M., Guerrero, M., and M. L. Amsler (2014),
1048 Estimation of Concentration and Load of Suspended Sediment in a Large River by Means
1049 of Doppler Technology, *J. Hydraul. Eng.*, 140(7), Article number 04014023.

1050 Lee, H.-Y., and I.-S. Hsu (1994), Investigation of saltating particle motions. *J. Hydraul. Eng.*,
1051 120(7), 831–845.

1052 Leite Ribeiro, M., Blanckaert, K., Roy, A. G., and A. J. Schleiss (2012), Flow and sediment
1053 dynamics in channel confluences, *J. Geophys. Res.: Earth Surf.*, 117(1), F01035,
1054 doi:10.1029/2011JF002171.

1055 Lemmin, U., and T. Rolland (1997), Acoustic velocity profiler for laboratory and field
1056 studies, *J. Hydr. Eng.*, 123(12), 1089–1098.

1057Lhermitte, R., and R. Serafin (1984), Pulse-to-pulse coherent Doppler sonar signal processing
1058 techniques, *J. Atm. Ocean. Tech.*, 1(4), 293-308.

1059Lucas, B. D., and T. Kanade (1981), An Iterative Image Registration Technique with an
1060 Application to Stereo Vision, *Proc. of 7th Int. Joint Conf. on Artificial Intelligence*,
1061 Vancouver, Canada, 674–679.

1062Martin, R. L., Jerolmack, D. J., and R. Schumer (2012), The physical basis for anomalous
1063 diffusion in bed load transport, *J. Geophys. Res.: Earth Surf.*, 117(1), F01018.

1064Mettra, F. (2014), Morphodynamic mechanisms in steep channels: from local processes to
1065 large-scale evolution. PhD thesis no 6065, EPFL, Lausanne, Switzerland.

1066Miller, K. S., and M. M. Rochwarger (1972), Covariance approach to spectral moment
1067 estimation, *IEEE Trans. Inform. Theory*, 18(5), 588-596.

1068Moore, S. A., Le Coz, J., Hurther, D., and A. Paquier (2013), Using multi-frequency acoustic
1069 attenuation to monitor grain size and concentration of suspended sediment in rivers, *J.*
1070 *Acoust. Soc. Am.*, 133(4), 1959-1970.

1071Mulhoffer L. (1933), Untersuchungen über der Schwebstoff und Geschiebeführung des Inn
1072 nächst Kirchbichl, Tirol [Investigations into suspended load and bedload of the River Inn,
1073 near Kirchbichl, Tirol], *Wasserwirtschaft*, Heft 1-6.

1074Muste, M., Yu, K., Fujita, I., and R. Ettema (2009), Two-phase flow insights into open-
1075 channel flows with suspended particles of different densities, *Env. Fluid Mech.*, 9(2), 161-
1076 186.

1077Naqshband, S., Ribberink, J. S., Hurther, D., Barraud P. A., and S. J. M. H. Hulscher (2014a),
1078 Experimental evidence for turbulent sediment flux constituting a large portion of the total
1079 sediment flux along migrating sand dunes, *Geophys. Res. Lett.*, 41(24), 8870-8878,
1080 doi:10.1002/2014GL062322.

1081Naqshband, S., Ribberink, J. S., Hurther, D., and S. J. M. H. Hulscher (2014b), Bed load and
1082 suspended load contributions to migrating sand dunes in equilibrium, *J. Geophys. Res.:*
1083 *Earth Surf.*, 119(5), 1043–1063, doi:10.1002/2013JF003043.

1084Nezu, I., and H. Nakagawa (1993), *Turbulence in Open Channel Flows*, 281 pp., A. A.
1085 Balkema, Rotterdam, Netherlands.

1086Nino, Y., and M. H. Garcia, M. H. (1996), Experiments on particle-turbulence interactions in
1087 the near-wall region of an open channel flow: Implications for sediment transport, *J. Fluid*
1088 *Mech.*, 326, 285-319.

1089Pinkel, R. (1980), Acoustic Doppler techniques, in *Air–Sea Interaction Instruments and*
1090 *Methods*, edited by F. Dobson et al., pp. 171–199, New York: Plenum Press.

1091Radice, A., Malavasi, S., and F. Ballio (2006), Solid transport measurements through image
1092 processing, *Exp. Fluids*, 41(5), 721-734.

1093Rennie, C. D., and M. Church (2010), Mapping spatial distributions and uncertainty of water
1094 and sediment flux in a large gravel bed river reach using an acoustic Doppler current
1095 profiler, *J. Geophys. Res.: Earth Surf.*, 115(3), F03035.

1096Rennie, C. D., and R. G. Millar (2007), Deconvolution technique to separate signal from
1097 noise in gravel bedload velocity data, *J. Hydraulic Eng.*, 133(8), 845-856.

1098Rennie, C. D., Millar, R. G., and M. A. Church (2002), Measurement of bed load velocity
1099 using an acoustic Doppler current profiler, *J. Hydraulic Eng.*, 128(5), 473-483.

1100Rennie, C. D., and P. V. Villard (2004), Site specificity of bed load measurement using an
1101 acoustic Doppler current profiler, *J. Geophys. Res.: Earth Surf.*, 109(F3), F03003.

1102Rolland, T., and U. Lemmin (1997), A Two-component Acoustic Velocity Profiler for Use in
1103 Turbulent Open-channel Flow, *J. Hydraul. Res.*, 35(4), 545–561.

1104Rogers, S. S., Waigh, T. A., Zhao, X., and J. R. Lu (2007), Precise particle tracking against a
1105 complicated background: polynomial fitting with Gaussian weight, *Phys. Biol.*, 4(3), 220-
1106 227.

1107Roseberry, J. C., Schmeeckle, M. W., and D. J. Furbish (2012), A probabilistic description of
1108 the bed load sediment flux: 2. Particle activity and motions, *J. Geophys. Res.: Earth Surf.*,
1109 117(3), F03032.

1110Ruhnau, P., Kohlberger, T., Schnörr, C., and H. Nobach (2005), Variational optical flow
1111 estimation for particle image velocimetry, *Exp. Fluids*, 38(1), 21-32.

1112Seizilles, G., Lajeunesse, E., Devauchelle, O., and M. Bak (2014), Cross-stream diffusion in
1113 bedload transport, *Phys. Fluids*, 26(1), 013302.

1114Shen, C., and U. Lemmin (1999), Application of an acoustic particle flux profiler in particle-
1115 laden open-channel flow, *J. Hydraulic Res.*, 37(3), 407-419.

1116Shields, A. (1936), Anwendung der Aehnlichkeitsmechanik und der Turbulenzforschung auf
1117 die Geschiebebewegung [Application of similarity mechanics and turbulence research on
1118 shear flow]. Mitteilungen der Preußischen Versuchsanstalt für Wasserbau (in German) 26.
1119 Berlin: Preußische Versuchsanstalt für Wasserbau.

1120Singh, A., Fienberg, K., Jerolmack, D. J., Marr, J., and E. Foufoula-Georgiou (2009),
1121 Experimental evidence for statistical scaling and intermittency in sediment transport rates,
1122 *J. Geophys. Res.: Earth Surf.*, 114(1),F01025.

1123Smyth, C., Hay, A. E., and L. Zedel (2002), Coherent Doppler Profiler measurements of near-
1124 bed suspended sediment fluxes and the influence of bed forms, *J. Geophys. Res.: Oceans*,
1125 107(C8), 19-1 - 19-20, doi: 10.1029/2000JC000760.

1126 Spies, H., Beringer O., Gröning, H., and H. Haussecker (1999), Analyzing particle
1127 movements at soil interfaces, in *Handbook on Computer Vision and Applications*, edited
1128 by B. Jähne et al., vol 3, 699-718, Academic Press.

1129 Stanton, T. P., and E. B. Thornton (1999), Sediment fluxes above a mobile sandy bed in the
1130 nearshore, *Coastal Sediments '99, Volume One, Proceedings of the 4th International*
1131 *Symposium on Coastal Engineering and Science of Coastal Sediment Processes*, 241-252.

1132 Stanton, T. P. (2001), Bistatic Doppler velocity and sediment profiler device for measuring
1133 sediment concentration, estimates profile of mass flux from the product of mass
1134 concentration and three component velocity vector, Us Sec of Navy. Patent number
1135 US6262942-B1.

1136 Thorne, P. D., and D. M. Hanes (2002), A review of acoustic measurement of small scale
1137 sediment processes, *Cont. Shelf Res.*, 22, 603-632.

1138 Thorne, P. D., and P. J. Hardcastle (1997), Acoustic measurements of suspended sediments in
1139 turbulent currents and comparison with in-situ samples, *J. Acoust. Soc. Am.*, 101(5), 2603-
1140 2614.

1141 Thorne, P. D., Hardcastle, P. J., and P. S. Bell (1998), Application of acoustics for measuring
1142 nearbed sediment processes: An integrated approach, *Oceans'98 - Conference*
1143 *Proceedings*, Vols 1-3, 438-441.

1144 Thorne, P. D., and D. Hurther (2014), An overview on the use of backscattered sound for
1145 measuring suspended particle size and concentration profiles in non-cohesive inorganic
1146 sediment transport studies, *Cont. Shelf Res.*, 73, 97-118.

1147 Thorne, P. D., Hurther, D., and B. D. Moate (2011), Acoustic inversions for measuring
1148 boundary layer suspended sediment processes, *J. Acoust. Soc. Am.*, 130(3), 1188-1200.

1149Traykovski, P. (1998), Observations and modeling of sand transport in a wave dominated
1150 environment, PhD thesis, Massachusetts Institute of Technology and Woods Hole
1151 Oceanographic Institution.

1152van Rijn, L. C. (1984), Sediment transport. Part I: bed load transport, *J. Hydraulic Eng.*,
1153 110(10), 1431-1456.

1154Williams, R. D., Rennie, C. D., Brasington, J., Hicks, D. M., and D. Vericat (2015), Linking
1155 the spatial distribution of bed load transport to morphological change during high-flow
1156 events in a shallow braided river, *J. Geophys. Res.: Earth Surf.*, 120(3), 604-622.

1157Wilson, G. W. , and A. E. Hay (2015), Acoustic backscatter inversion for suspended sediment
1158 concentration and size: A new approach using statistical inverse theory, *Continental Shelf*
1159 *Research*, 106, 130-149.

1160Wilson, G. W. , and A. E. Hay (2015), Measuring two-phase particle flux with a multi-
1161 frequency acoustic Doppler profiler, *Journal of the Acoustical Society of America*, 138(6),
1162 3811-3819.

1163Wright, S. A., Topping, D. T., and C. A. Williams (2010), Discriminating silt and clay from
1164 suspended sand in rivers using side-looking profilers. In *Proceedings of the 2nd Joint*
1165 *Federal Interagency Sedimentation Conference*, LasVegas, NV, USA, 27 June-1 July 2010.

1166Zedel, L., and A. E. Hay (2002), A three-component bistatic coherent Doppler velocity
1167 profiler: Error sensitivity and system accuracy, *IEEE J. Ocean. Eng.*, 27(3), 717-725.

1168Zedel, L., Hay, A. E., Cabrera, R., and A. Lohrmann (1996), Performance of a single-beam
1169 pulse-to-pulse coherent Doppler profiler, *IEEE J. Ocean. Eng.*, 21(3), 290-297.

1170

Figure Captions

1171

1172

1173**Figure 1:** Acoustic Doppler Velocity Profiler (ADVP) and digital video camera. The ADVP
1174consists of a central beam emitter surrounded by four receivers; only two receivers are shown
1175in the Figure. Theinsonified water column is divided in bins. The fan-beam receivers are
1176sensitive in a field with a wide opening angle, with maximum sensitivity along the receiver
1177axis. The red arcs define the ellipses of equal acoustic path travel time between the send and
1178receive transducers for the bed bin (bottom arc) and the first bin above the bed (top arc). (a)
1179Standard ADVP configuration optimized for flow measurements in the body of the water
1180column. The transducers are in a water-filled box that is separated from the flowing water by
1181an acoustically transparent mylar film. The fan-beam receivers cover the entire water column,
1182and the receiver axis is focused in the body of the water column. (b) ADVP configuration
1183optimized for bedload measurements. The transducers are immersed in the flowing water.
1184The fan-beam receivers only cover the lower half of the water column, and the receiver axis
1185is focused on the bed level. (c) Simultaneous deployment of the ADVP optimized for bedload
1186measurements and a digital video camera focused on the same near-bed sample volume.

1187

1188**Figure 2:** Time-averaged magnitude of the backscattered raw return signal recorded by the
1189receive transducers, I^2 [V^2], for the Q795L experiment with low acoustic power (blue, x) and
1190the Q795H experiment with high acoustic power (red, o). The configuration with high
1191acoustic power optimizes the signal-to-noise ratio in the water column but provides a
1192magnitude of the backscattered signal that is frequently outside the recording range of the
1193receivers in the bedload layer. The configuration with low acoustic power provides a
1194backscattered signal that remains within the recording range of the receivers in the bedload
1195layer. The vertical axis to the left is the bin number, which increases with distance from the
1196ADVP. The vertical axis to the right is the distance above the surface of the immobile bed.
1197The full black horizontal line indicates the assumed level of the surface of the immobile bed,
1198the dashed brown horizontal line the top of the assumed layer of rolling and sliding bedload,
1199and the dotted black horizontal line the top of the layer of saltating bedload. ADVP
1200measurements in bin numbers smaller than 37 are outside the sensitivity range of the ADVP
1201transducers for the present ADVP configuration.

1202

1203

1204**Figure 3:** Time-averaged ADVP profiles of the longitudinal velocity estimated with the
1205 pulse-pair algorithm (Equation 4). The dashed line represents a linear fitting of the measured
1206 velocity against $\log(30z/k_s)$. The distance (m) above the immobile bed is indicated by z , and
1207 the equivalent grain roughness k_s is taken as 0.01 m. In order to avoid singularities, the bin
1208 containing the surface of the immobile bed has been plotted at $z = 0.001$ m. (a) Experiments
1209 in the second series of test with nominal flow depth of 0.14 m (Table 1); (b) Experiment
1210 Q795L in the main series of experiment. The symbol (v) denotes experiments without
1211 bedload sediment transport, and the symbol (x) denotes experiments with bedload sediment
1212 transport.

1213

1214**Figure 4:** Near-bed bins including the bin in which the surface of the immobile bed is
1215 situated. The upper part of that bin is situated in the flow where bedload sediment particles
1216 roll and slide on the bed. Therefore the bin containing the surface of the immobile bed is
1217 identified as the bin with minimum non-zero velocity measured by the ADVP. Figure on scale

1218

1219**Figure 5:** Temporal evolution of the magnitude of the raw backscattered signal, I^2 [V^2],
1220 during the 614 s Q1000L experiment. The colorbar defines the scale of I^2 . The vertical axis
1221 shows the part of the water column between bin numbers 50 and 65 where the magnitude
1222 reaches maximum values. The 614 s duration is divided in five periods of quasi-constant
1223 conditions. Digital videography was performed during sequences of 10 s with an interval of
1224 60 s, as indicated by the labels V1 to V11.

1225

1226**Figure 6:** In-phase component I [V] of the complex range gated backscattered raw return
1227 signal measured at PRF = 1000 Hz by one of the receivers in the Q795L experiment from $t =$
1228 2 s to 2.2 s after the beginning of the experiment.

1229

1230**Figure 7:** Power spectral density of the four beam velocities in bins [3, 2, 1] above the bin
1231that contains the surface of the immobile bed in the Q795L experiment. Velocity [m s^{-1}] on
1232the abscissa is calculated from observed beam Doppler frequencies, and transformed to the
1233horizontal component.

1234

1235**Figure 8:** Time series of velocities sampled at a frequency of $\text{PRF/NPP} = 31.25$ Hz in the
1236Q795L experiment in bins 54 and 55 (clear water), 56 (saltating bedload layer), 57 (rolling
1237and sliding bedload layer), and 58 (containing the surface of the immobile-bed).

1238

1239**Figure 9:** Results of time-averaged velocities measured with ADV (profiles) and particle
1240tracking videography (gray distribution functions) for experiments Q630 (top row), Q795
1241(middle row) and Q1000 (bottom row). Test with low (left column) and high (right column)
1242acoustic power. Experiments have been divided into periods of quasi-homogeneous
1243conditions (Table 1 and Table S1 in the supporting information; period 1: blue, period 2:
1244green, period 3: black; period 4: cyan, period 5: mauve). Note that the horizontal axis only
1245refers to the time-averaged velocities measured with ADV, but has no relation to the
1246distribution function based on the videography.

1247

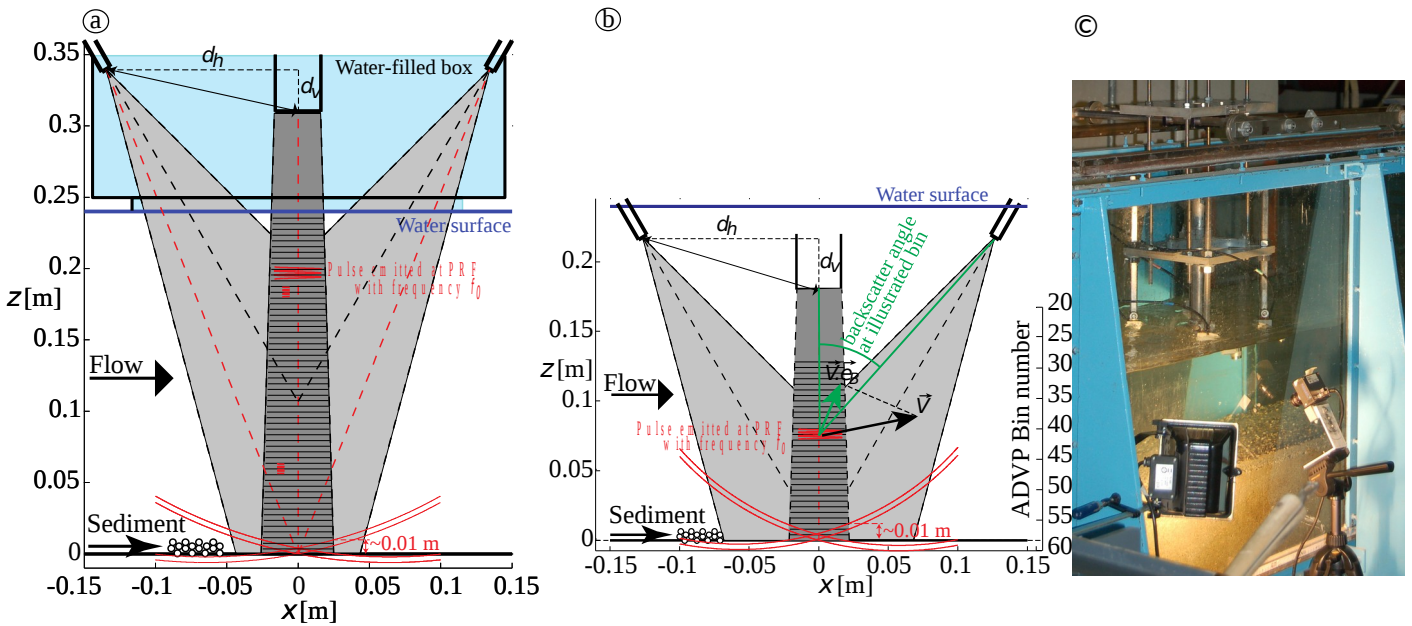
1248**Figure 10:** Time series of quasi-instantaneous velocities, including turbulent fluctuations,
1249measured with ADV in the bin containing the immobile bed and the bin just above (Figure 9
1250and Table 1) and estimated from the videography with the Optical Flow algorithm (thick red
1251line) for experiments Q630L (top row), Q795L (middle row) and Q1000L (bottom row). The
1252horizontal axis indicates time from the beginning of the experiment. Two 10 s sequences of
1253videography are shown (Figure 5). Additional videos showing the bedload transport are
1254provided online as supporting information.

1255

1256**Figure 11:** a) Sediment velocity in the bed load layer as a function of the shear velocity u_* .
1257measured with ADV (black) and estimated from videos by PTV (grey). The two lines
1258represent predictions according to Equation 7 for $a = 4.4$ and $a = 13.2$, respectively. b)
1259Thickness of the layer of rolling and sliding bedload (indicated in Figure 9) estimated from

1260ADVP as a function of the shear velocity u_* . The two lines represent prediction according to
1261Equation 8 for $d = d_{50} = 0.0008$ m and $d = 0.0015$ m. For both a) and b), circles represent the
1262experiments with simultaneous videography (main series), squares the second series
1263experiments with flow depth 0.14 m, and crosses the second series experiments with flow
1264depth 0.24 m. Because results for different periods within the same experiment were not
1265significantly different, only one data point per experiment is shown, obtained as the average
1266of results of all periods.

1
2



3

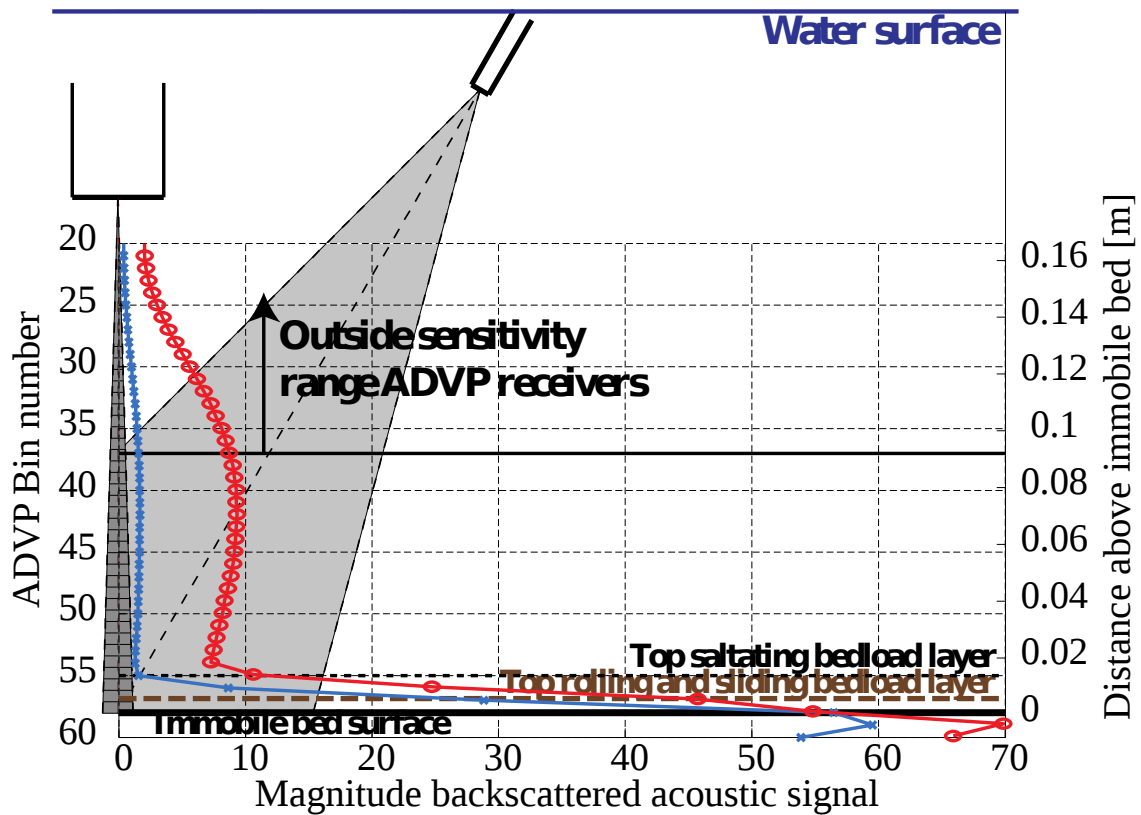
4Figure 1: Acoustic Doppler Velocity Profiler (ADVP) and digital video camera. The ADVP consists of a
5central beam emitter surrounded by four receivers; only two receivers are shown in the Figure. The insonified
6water column is divided in bins. The fan-beam receivers are sensitive in a field with a wide opening angle, with
7maximum sensitivity along the receiver axis. The red arcs define the ellipses of equal acoustic path travel time
8between the send and receive transducers for the bed bin (bottom arc) and the first bin above the bed (top arc).

9(a) Standard ADVP configuration optimized for flow measurements in the body of the water column. The
10transducers are in a water-filled box that is separated from the flowing water by an acoustically transparent
11mylar film. The fan-beam receivers cover the entire water column, and the receiver axis is focused in the body
12of the water column. (b) ADVP configuration optimized for bedload measurements. The transducers are
13immersed in the flowing water. The fan-beam receivers only cover the lower half of the water column, and the
14receiver axis is focused on the bed level. (c) Simultaneous deployment of the ADVP optimized for bedload
15measurements and a digital video camera focused on the same near-bed sample volume.

16

17

18



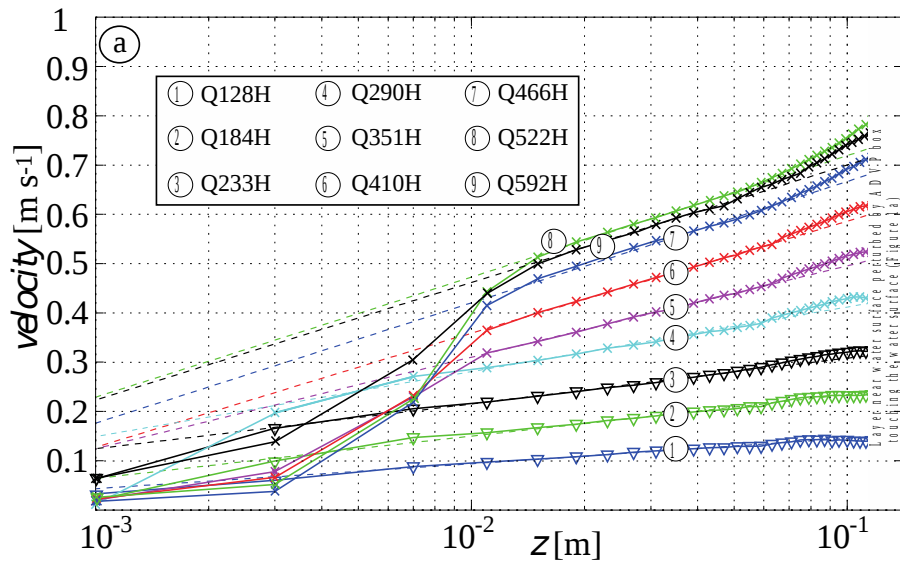
19

20

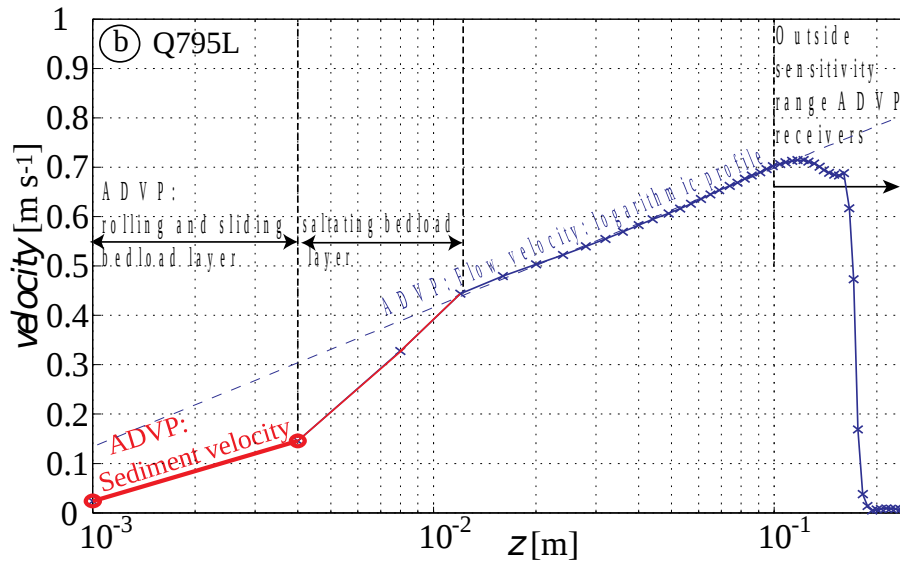
21**Figure 2:** Time-averaged magnitude of the backscattered raw return signal recorded by the receive transducers,
 22 I^2 [V^2], for the Q795L experiment with low acoustic power (blue, x) and the Q795H experiment with high
 23acoustic power (red, o). The configuration with high acoustic power optimizes the signal-to-noise ratio in the
 24water column but provides a magnitude of the backscattered signal that is frequently outside the recording
 25range of the receivers in the bedload layer. The configuration with low acoustic power provides a backscattered
 26signal that remains within the recording range of the receivers in the bedload layer. The vertical axis to the left
 27is the bin number, which increases with distance from the ADVP. The vertical axis to the right is the distance
 28above the surface of the immobile bed. The full black horizontal line indicates the assumed level of the surface
 29of the immobile bed, the dashed brown horizontal line the top of the assumed layer of rolling and sliding
 30bedload, and the dotted black horizontal line the top of the layer of saltating bedload. ADVP measurements in
 31bin numbers smaller than 37 are outside the sensitivity range of the ADVP transducers for the present ADVP
 32configuration.

33

34
35



36
37

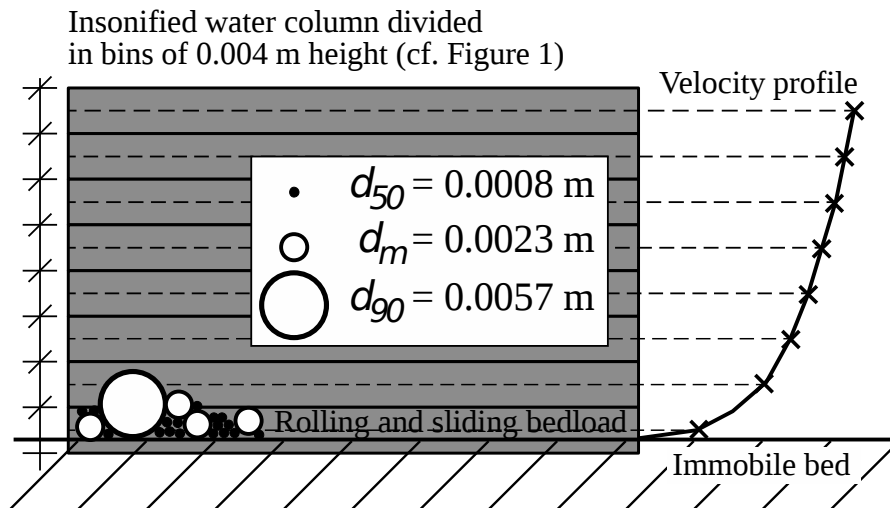


38
39
40
41

42 **Figure 3:** Time-averaged ADVP profiles of the longitudinal velocity estimated with the pulse-pair algorithm
 43 (Equation 4). The dashed line represents a linear fitting of the measured velocity against $\log(30z/k_s)$. The
 44 distance in meter above the immobile bed is indicated by z , and the equivalent grain roughness k_s is taken as
 45 0.01 m . In order to avoid singularities, the bin containing the surface of the immobile bed has been plotted at z
 46 $= 0.001 \text{ m}$. (a) Experiments in the second series of test with nominal flow depth of 0.14 m (Table 1); (b)
 47 Experiment Q795L in the main series of experiment. The symbol (v) denotes experiments without bedload
 48 sediment transport, and the symbol (x) denotes experiments with bedload sediment transport.

49

50
51



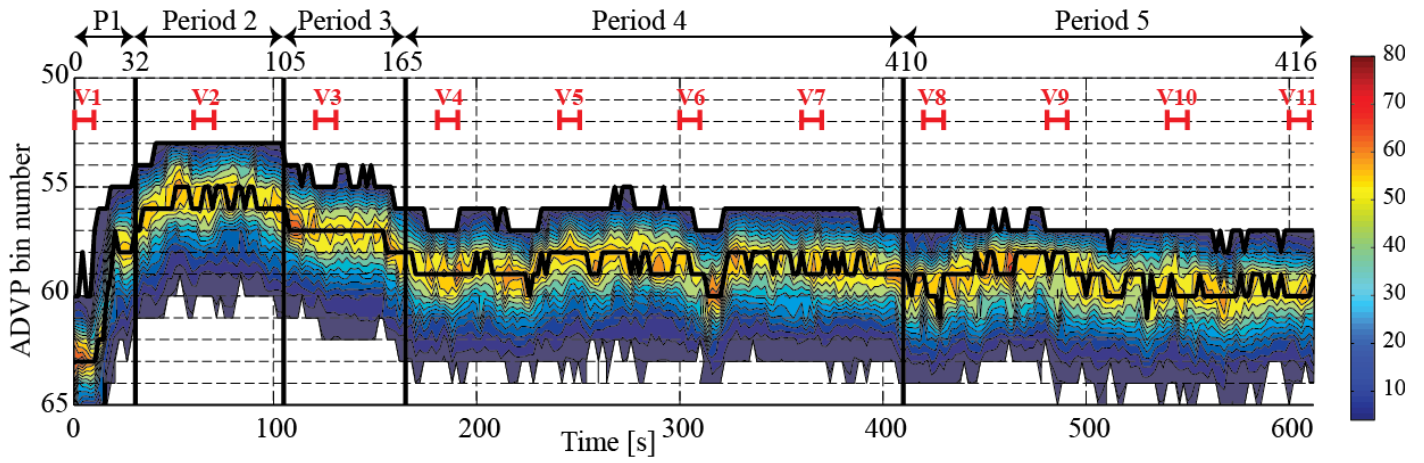
52
53
54
55

56Figure 4: Near-bed bins including the bin in which the surface of the immobile bed is situated. The upper part
57of that bin is situated in the flow where bedload sediment particles roll and slide on the bed. Therefore the bin
58containing the surface of the immobile bed is identified as the bin with minimum non-zero velocity measured
59by the ADV. Figure on scale

60
61
62
63

64

65



66

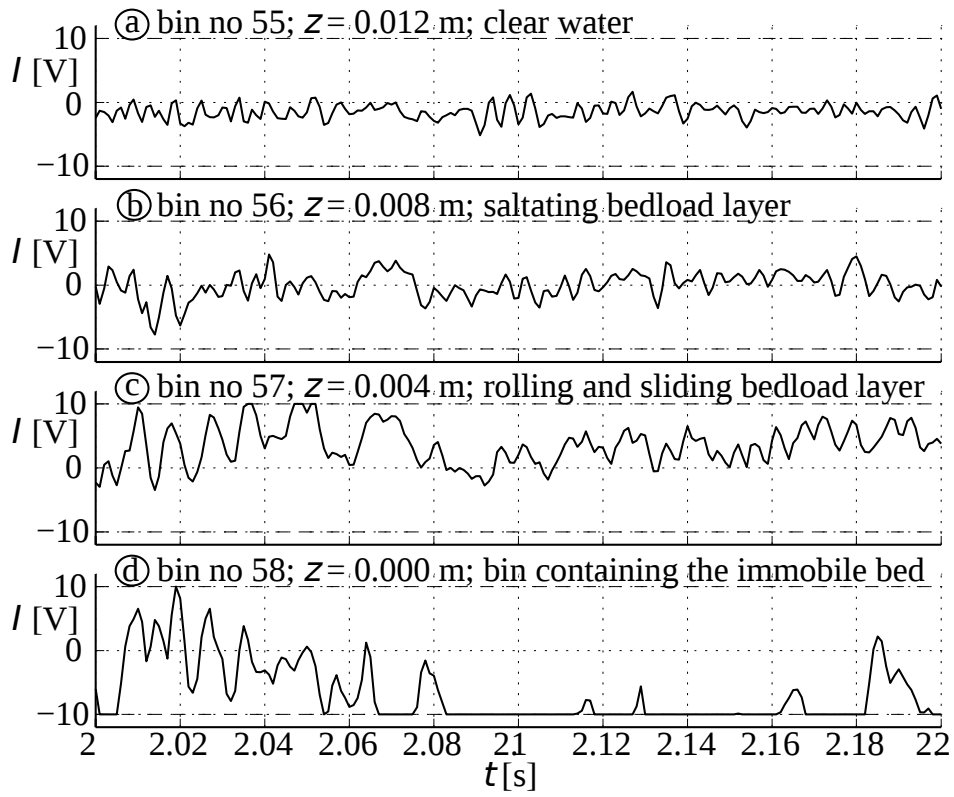
67

68**Figure 5:** Temporal evolution of the magnitude of the raw backscattered signal, I^2 [V^2], during the 614 s
69Q1000L experiment. The colorbar defines the scale of I^2 . The vertical axis shows the part of the water column
70between bin numbers 50 and 65 where the magnitude reaches maximum values. The 614 s duration is divided
71in five periods of quasi-constant conditions. Digital videography was performed during sequences of 10 s with
72an interval of 60 s, as indicated by the labels V1 to V11.

73

74

75



76

77

78**Figure 6:** In-phase component I [V] of the complex range gated backscattered raw return signal measured at
79PRF =1000 Hz by one of the receivers in the Q795L experiment from $t = 2$ s to 2.2 s after the beginning of the
80experiment.

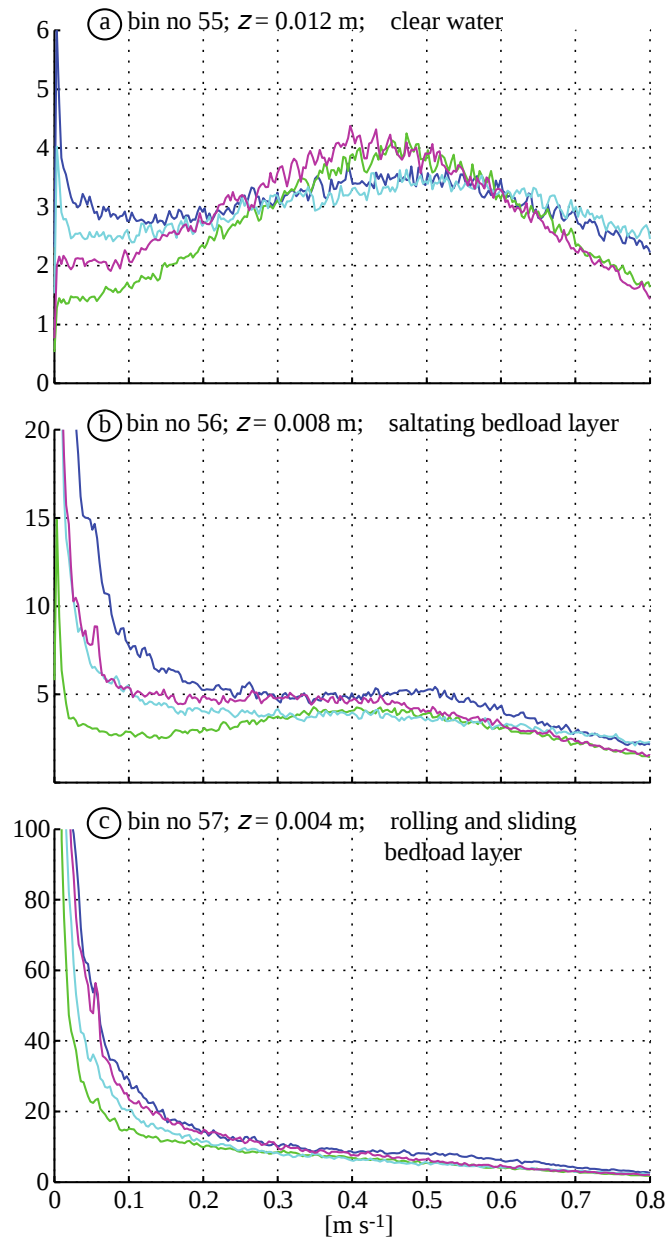
81

82

83

84

85



86

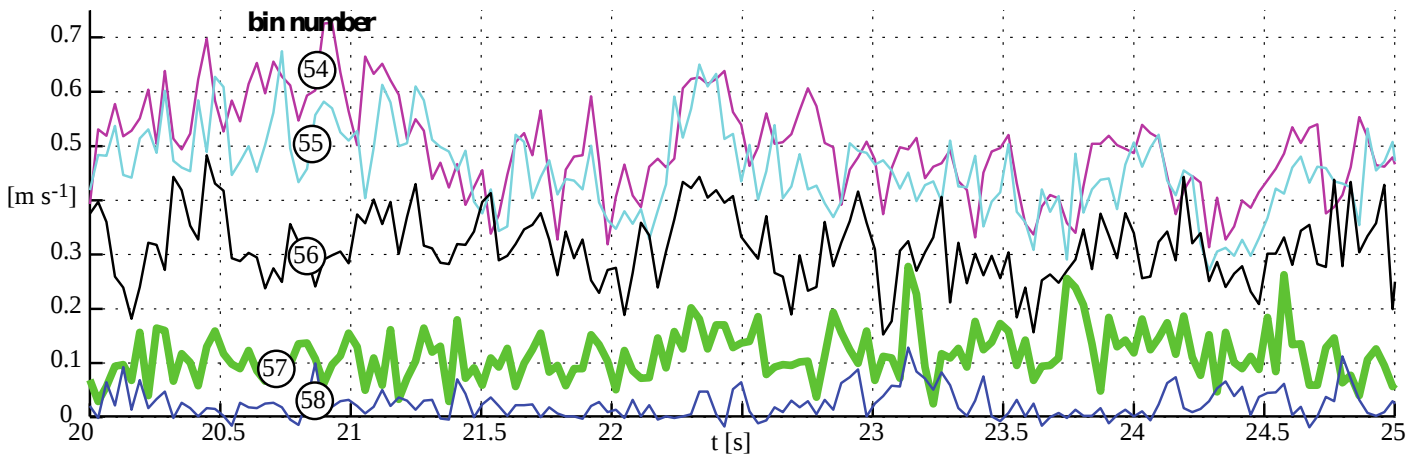
87

88**Figure 7:** Power spectral density of the four beam velocities in bins [3, 2, 1] above the bin that contains the
89surface of the immobile bed in the Q795L experiment. Velocity [m s^{-1}] on the abscissa is calculated from
90observed beam Doppler frequencies, and transformed to the horizontal component.

91

92

93



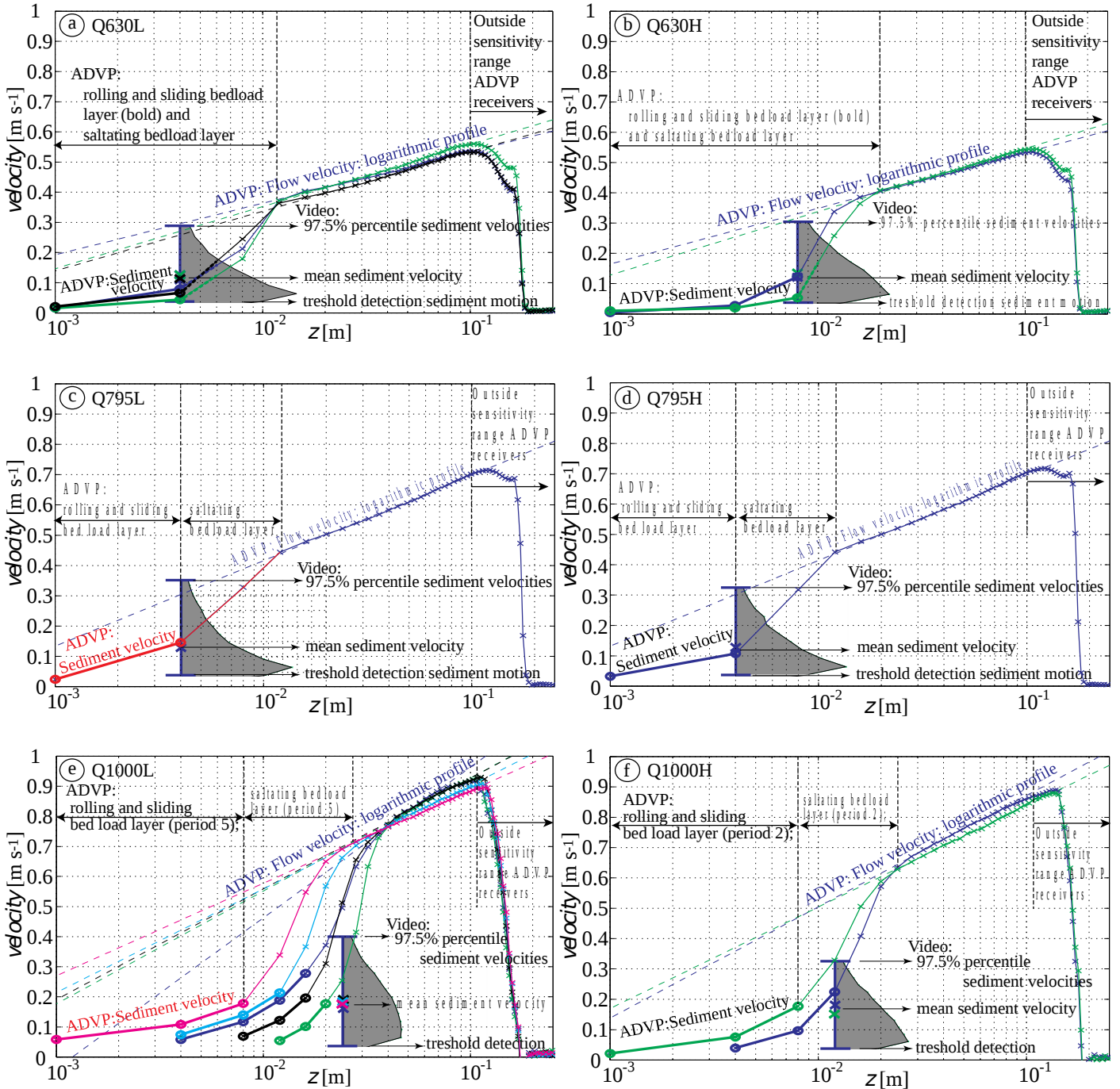
94

95

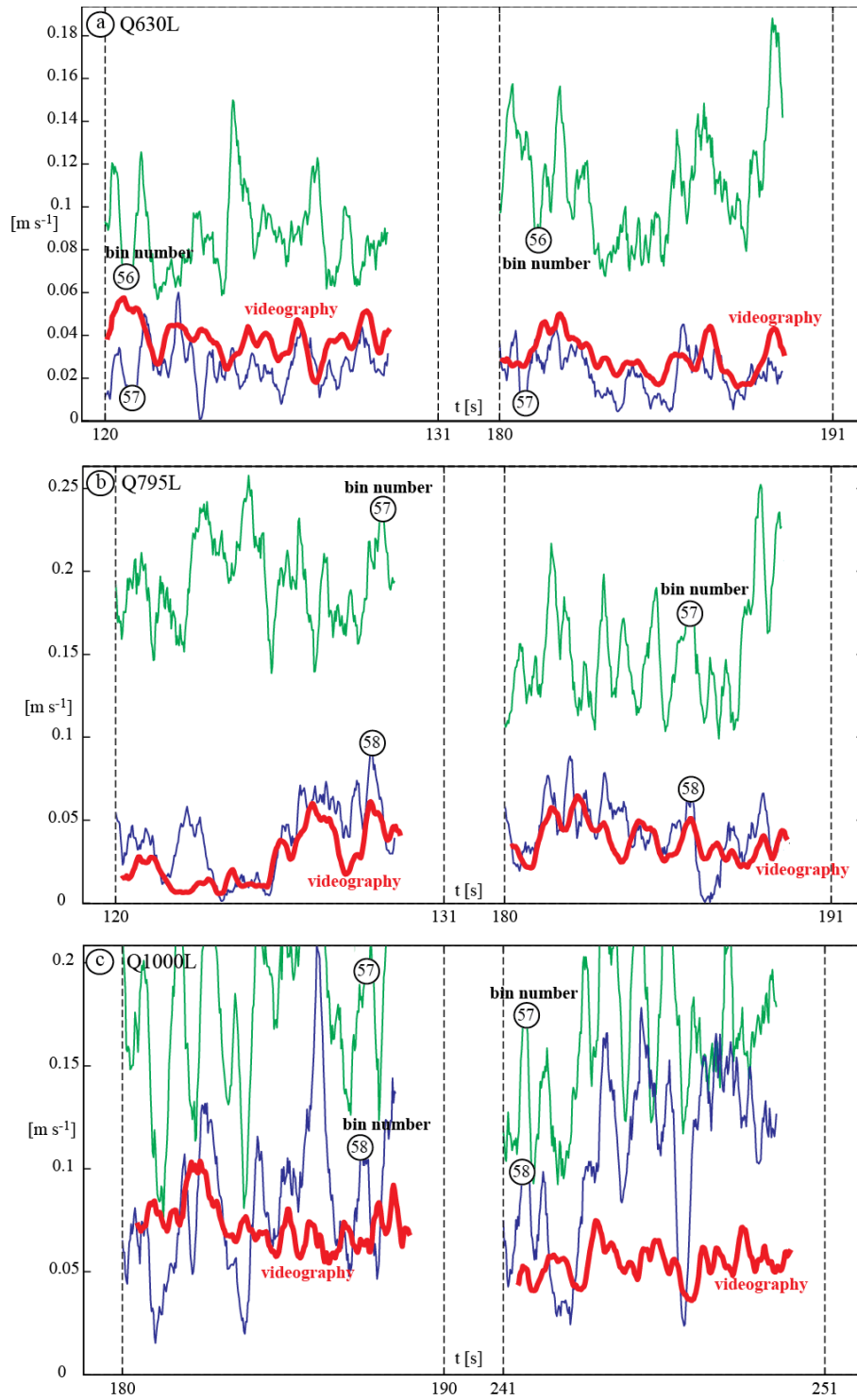
96**Figure 8:** Time series of velocities sampled at a frequency of $PRF/NPP = 31.25$ Hz in the Q795L experiment in
97bins 54 and 55 (clear water), 56 (saltating bedload layer), 57 (rolling and sliding bedload layer), and 58
98(containing the surface of the immobile-bed).

99

100

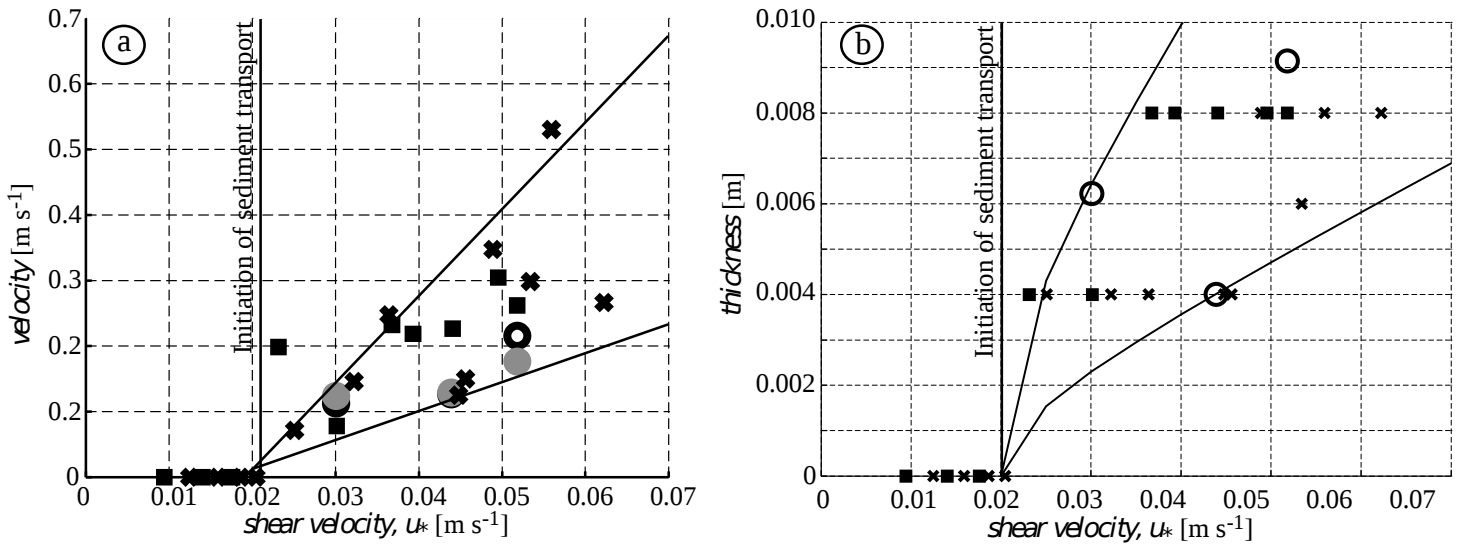


101 **Figure 9:** Results of time-averaged velocities measured with ADVP (profiles) and particle tracking videography
 102 (gray distribution functions) for experiments Q630 (top row), Q795 (middle row) and Q1000 (bottom row). Test
 103 with low (left column) and high (right column) acoustic power. Experiments have been divided into periods of
 104 quasi-homogeneous conditions (Table 1 and Table S1 in the supporting information; period 1: blue, period 2:
 105 green, period 3: black; period 4: cyan, period 5: mauve). Note that the horizontal axis only refers to the time-
 106 averaged velocities measured with ADVP, but has no relation to the distribution function based on the
 107 videography.



108

109 **Figure 10:** Time series of quasi-instantaneous velocities, including turbulent fluctuations, measured with ADVP
 110 in the bin containing the immobile bed and the bin just above (Figure 9 and Table 1) and estimated from the
 111 videography with the Optical Flow algorithm (thick red line) for experiments Q630L (top row), Q795L (middle
 112 row) and Q1000L (bottom row). The horizontal axis indicates time from the beginning of the experiment. Two
 113 10 s sequences of videography are shown (Figure 5). Additional videos showing the bedload transport are
 114 provided online as supporting information.



117 **Figure 11:** a) Sediment velocity in the bed load layer as a function of the shear velocity u_* , measured with
 118 ADVP (black) and estimated from videos by PTV (grey). The two lines represent predictions according to
 119 Equation 7 for $a = 4.4$ and $a = 13.2$, respectively. b) Thickness of the layer [of rolling and sliding bedload](#)
 120 [\(indicated in Figure 9\)](#) estimated from ADVP as a function of the shear velocity u_* . The two lines represent
 121 prediction according to Equation 8 for $d = d_{50} = 0.0008$ m and $d = 0.0015$ m. For both a) and b), circles
 122 represent the experiments with simultaneous videography (main series), squares the second series experiments
 123 with flow depth 0.14 m, and crosses the second series experiments with flow depth 0.24 m. Because results for
 124 different periods within the same experiment were not significantly different, only one data point per
 125 experiment is shown, obtained as the average of results of all periods.